TOOL FOR TERAHERTZ DEVICE DEVELOPME

Final Report
(April 2000 - October 2000)

by
P. Stout, W. Yuan, C. Wordelman, and A. J. Przekwas
CFD Research Corporation

CFD Research Corporation
CFDRC

CAD TOOL FOR TERAHERTZ DEVICE DEVELOPMENT

Final Report
(April 2000 - October 2000)

by
P. Stout, W. Yuan, C. Wordelman, and A. J. Przekwas
CFD Research Corporation

G. Klimeck
Jet Propulsion Laboratory

S. J. Allen
University of California, Santa Barbara

R. C. Bowen
Texas Instruments

R. Lake
University of California, Riverside

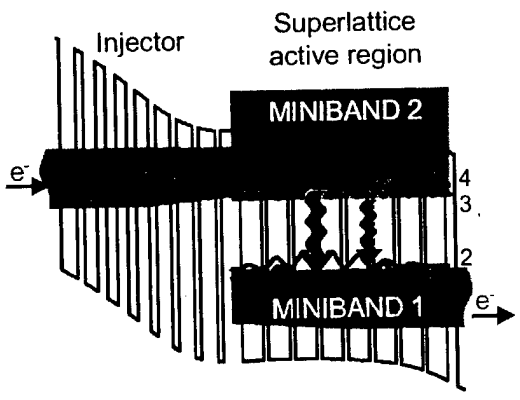

superlattice QCL

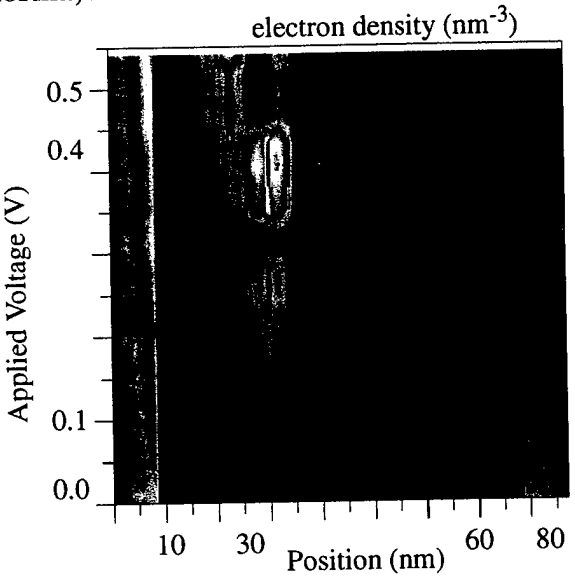

October 2000

CFDRC Report: 8278/2

Sponsored by
Defense Advanced Research Projects Agency/MTO
ARPA Order D611/79

CFD Research Corporation
215 Wynn Dr. • Huntsville, Alabama 35805 • Tel.: (256) 726-4800 • FAX: (256) 726-4806 • info@cfdrc.com

CAD TOOL FOR TERAHERTZ DEVICE DEVELOPMENT

Final Report
(April 2000 - October 2000)

by

P. Stout, W. Yuan, C. Wordelman, and A. J. Przekwas
CFD Research Corporation

G. Klimeck
Jet Propulsion Laboratory

S. J. Allen
University of California, Santa Barbara

R. C. Bowen
Texas Instruments

R. Lake
University of California, Riverside

October 2000

CFDRC Report: 8278/2

Sponsored by
Defense Advanced Research Projects Agency/MTO
ARPA Order D611/79

Issued by
U.S. Army Aviation and Missile Command (AMCOM)
Contract Number: DAAH01-00-C-R120

CFD Research Corporation

215 Wynn Dr. • Huntsville, Alabama 35805 • Tel.: (256) 726-4800 • FAX: (256) 726-4806 • info@cfdrc.com

CFDRC

December 19, 2000

Mr. William A. Friday
U.S. Army Aviation and Missile Command
Attn: AMSAM-RD-WS-DP-SB
Bldg. 7804, Room 205
Redstone Arsenal, AL 35898

SUBJECT: Final Report for "CAD Tool for Terahertz Device Development," Contract Number: DAAH01-00-C-R120; CFDRC Project Number: 8278

Dear Mr. Friday,

Enclosed please find two copies of the above mentioned final report. If you have any questions or require further information, please do not hesitate to contact me at any time.

Sincerely,

Phillip Stout
Senior Research Engineer/Advanced Technology

PJS/src/8278/2

Enclosure

TABLE OF CONTENTS

EXECUTIVE SUMMARY

The overall objective of this project is to develop a commercial quality, validated computer aided design (CAD) tool, THz quantum based semiconductor devices. THz device design must account for quantum effects such as quantum resonant modes, quantum mode mixing, tunneling, intersubband transitions, side wall scattering, and surface recombination. Currently, there are no CAD tools available that incorporate all the proper physics for designing THz quantum devices. The proposed quantum CAD tool will be a device simulator with the ability to investigate the operation of and generate reduced models (S-parameters) for quantum based, electronic and photonic THz sources and detectors such as quantum cascade lasers, superlattices, and multiple quantum wells.

The objective of this Phase I proof of the concept project is to determine the current capabilities and future development needs of the Quantum device simulator, NEMO, for modeling quantum based terahertz devices. In Phase I, an existing quantum simulator, NEMO, has been coupled to a drift-diffusion model to enable multi-scale studies of semiconductor devices. The quantum device simulator linked to a classical model has been demonstrated and verified on RTDs, superlattices, and QCLs with varying levels of success. Finally, the tool was further integrated into CFDRC's commercial microelectronics CAD environment by converting the GUI to FOX (a CFDRC GUI library technology).

The approach taken for solving drift-diffusion in the terminals is to use a calculated current and carrier density to determine the gradient of the fermi-level across the terminals. The fermi level is initially fixed at the emitter and collector boundaries. This is a typical approach when heterostructures are in the semiconductor device because the fermi level is piece-wise continuous when the carriers can be characterized by a fermi-level. The formulation is currently only for electrons and does not include recombination or generation effects. The drift-diffusion (DD) implementation was demonstrated on a GaAs/$Al_{0.4}Ga_{0.6}As$ RTD. The inclusion of DD is seen to effect the fermi level near the collector region for the cases shown. The fermi-level's effect of increasing the carrier density in the collector region was also shown. Decreasing the doping level and the electron mobility is seen to increase the effect (the fermi-level deviation from the flat band) of DD in the terminals.

The equilibrium characteristics of a InAs/AlSb superlattice based device being developed at the University of California at Santa Barbara (UCSB) were calculated. The conduction band edge, fermi level, carrier density, electric potential, and electric field were calculated at zero bias (equilibrium). The carrier levels increased in the highly doped regions which occurred every eighth period in the superlattice design. This increase in carrier density pulled up the negative potential causing an oscillating electric potential and electric field in the superlattice with a period of eight superlattice periods.

Important capabilities that would allow NEMO to model THz devices are incoherent transport thorough multiple quantum wells and improvements in the material database. NEMO can currently model only coherent transport. Also the material database is missing parameters for higher order band structure models for different materials. Other material systems have out of date values or guesses. A study was carried out on the Quantum Cascade Laser (QCL) to highlight

future development requirements. This is an important terahertz device and will be a long-term goal for NEMO to model. The gamma conduction band minimum energy and electric potential were calculated at different bias points and different spatial regions of the device.

Finally, the process has begun to integrate NEMO into CFDRCs CAD environment. The first issue is updating the Graphical User Interface (GUI). The GUI used Motif and third party Motif widget sets (xrt-pdf) for plotting and table routines. The GUI is being transitioned to use the open-source FOX libraries (www.cfdrc.com/FOX/fox.html). This will lower CFDRC support costs and allow ports to the windows platforms.

ACKNOWLEDGEMENTS

This project was funded by the DARPA SBIR program and monitored by the US Army. The authors would like to thank Edgar Martinez and William Friday for their support of this work.

First, this work would not have been possible without the participation and knowledge of other institutions and members of the original NEMO team. This project would not have been realized without Raytheon's willingness to partner with CFDRC to commercialize the NEMO technology. The efforts of Gerhard Klimeck (Jet Propulsion Laboratory) and R. Chris Bowen (Texas Instruments) in implementing the AC small signal analysis and drift/diffusion in the terminals and advice on NEMO construction is appreciated. Also, Roger Lake's (University of California Riverside) on NEMO theory is appreciated.

Secondly, the willingness of S. J. Allen at the University of California Santa Barbara to share their experimental data to help validate the codes being developed here is greatly appreciated.

Finally, the authors would like to thank Mrs. Stephanie Cameron for preparing all of the reports and correspondence for this project as well as this final report.

1. INTRODUCTION

This is the final report describing the technical progress of a 6 month Phase I SBIR for a US Army / DARPA Research Project (Contract # DAAH01-00-C-R120) entitled "CAD Tool for Terahertz Device Development". The overall objective of this effort is to develop a commercial quality, validated computer aided design (CAD) tool to aid in the development of THz quantum based semiconductor devices. THz device design must account for quantum effects such as quantum resonant modes, quantum mode mixing, tunneling, intersubband transitions, side wall scattering, and surface recombination. Currently, there are no CAD tools available that incorporate all the proper physics for designing THz quantum devices. The proposed quantum CAD tool will be a device simulator with the ability to investigate the operation of and generate reduced models (S-parameters) for quantum based, electronic and photonic THz sources and detectors such as quantum cascade lasers, superlattices, and multiple quantum wells.

In Phase I, an existing quantum simulator, NEMO, has been coupled to a drift-diffusion model to enable multi-scale studies of semiconductor devices. The quantum device simulator linked to a classical model has been demonstrated and verified on RTDs, superlattices, and QCLs with varying levels of success. Finally, the tool was further integrated into CFDRC's commercial microelectronics CAD environment by converting the GUI to FOX (a CFDRC GUI library technology).

1.1 Terahertz Devices

THz devices, or more specifically sources, detectors, and circuits in the 0.3 THz to 10 THz region of the electromagnetic spectrum, offer a large set of potential applications such as trace gas analysis (pollution control, breath analysis, chemical and biological toxin detection on battlefield), new point-to-point communication systems (secure battlefield, space based), short range object detection (collision avoidance, battlefield characterization), night vision, and spectroscopy. However, as shown in Figure 1-1 there a few devices that operate in this region of the electromagnetic spectrum. The Terahertz region of the spectrum has historically been difficult to design for. This problem region begins where semiconductor devices based on diffusive electron transport reach their frequency limit. The upper limit is set by the transient time and the parasitic RC time constants. Given electron mobility values and the smallest feature size the upper limit is several hundred GHz. The problem region ends at the lower frequency limit of semiconductor devices based on quantum mechanical interband transitions. The limit is set by frequencies higher than frequencies corresponding to the semiconductor energy gap, which is higher than 10 THz for most bulk semiconductors.

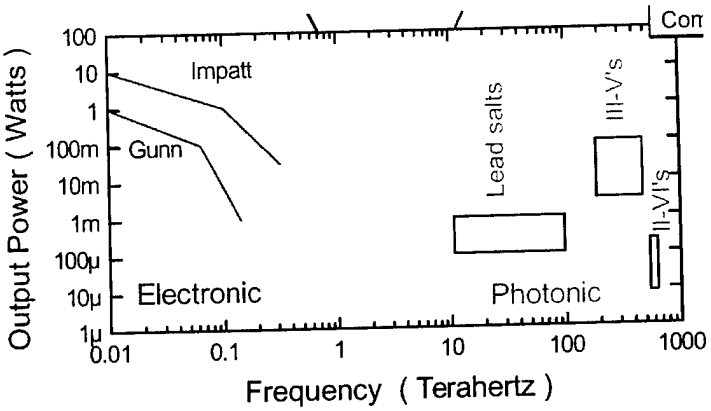

Figure 1-1. There exists a range of frequencies in the THz region where few devices exist. (illustration from the Center for Terahertz Science and Technology, UC Santa Barbara)

Recent strides in nanoelectronics are enabling devices to be designed for the Terahertz spectrum. These nanoelectronic devices use quantum mechanical effects based on device size and intersubband transitions (electrons making energy transitions between subband levels within the conduction band) to achieve devices in the THz frequency range. Because of difficulties in epitaxial material growth and the unfavorable fast nonradiative relaxation rate these quantum well based devices have only recently been developed (they were proposed in the 1970s, for example [Kazarinov et. al., 1971]). Some of these devices include Resonant Tunneling Diodes (RTDs) [M. Reddy et. al., 1997], Superlattice detectors and sources [Q. Hu et. al., 1998], Quantum Cascade Lasers (QCLs) [Capasso et. al., 1999], and Quantum Well Infrared Photodetectors (QWIPs) [Beck and Faska, 1996].

Resonant Tunneling Diodes (RTDs)

In resonant tunneling diodes, negative differential resistance (NDR) can be achieved at room temperature. Multiple quantum wells are engineered in the device to provide resonant states for carriers being transported through the device. A typical 2-barrier RTD consists of two semiconductor barriers embedded in a lower band-gap material (Figure 1-2a). To understand the basic operation of the RTD, one can consider the conduction bands to form a simple 1-dimensional potential for the carrier electrons. When the quasi-Fermi level in the emitter contact coincides with the energy of the quasi-bound state in the quantum well, electrons tunnel resonantly through the semiconductor barriers. Increased bias shifts the quasi-Fermi level above the quasi-bound state. This causes a peak in the device current (Figure 1-2b). Without an intermediate state to transmit the electrons, the current drops dramatically, forming a NDR region. As the bias increases further, more transmission through higher quasi-bound states or over the potential barriers causes the current to start increasing again. Scattering processes due to phonons or defects also contribute incoherent components to the current.

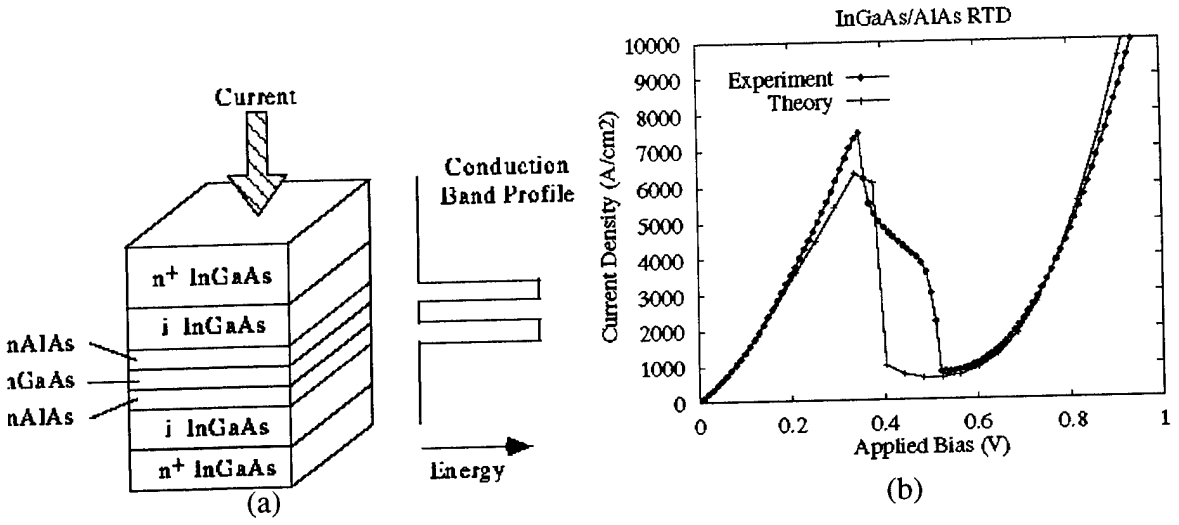

Figure 1-2. (a) Resonant tunneling diode with two InAlAs barriers and an InGaAs well. (b) Comparison of calculation (NEMO) of current versus voltage of InGaAs/InAlAs RTD with experimental data.

While the above explanation captures the essential RTD features, in practice it is quite challenging to accurately calculate the electronic characteristics of an RTD. The resonant electrons transmit at energies significantly higher than the conduction band edge of the well material. The parabolic band model often breaks down at these energies and the effect of multiple energy bands can have a significant effect on the current flow. The barrier material has an imaginary band structure component which must be taken into account for tunneling carriers. The open boundary conditions and scattering effects also add serious complications to the analysis. For these reasons, simulations prior to the creation of NEMO were extremely inaccurate. Calculated currents often differed from experimental results by several orders of magnitude, particularly in the valley current minimum where incoherent scattering and band structure effects dominate. In addition to these theoretical complications, typical quantum device simulations required excessive amounts of computing power and time.

Superlattice Detectors and Emitters

Other devices which rely on multiple quantum wells and intersubband transitions are detectors and emitters of THz radiation. Shown in Figure 1-3 are band profiles highlighting the device design and operation of electrically and optically pumped superlattices.

The electrically pumped device is a three energy level system based on a triple quantum well structure. The radiation transition takes place between E_3 and E_2, and the fast LO-phonon emission keeps the level E_2 empty. The optically pumped device is a four energy level system based on a coupled triple quantum-well structure. Electrons can be pumped from the E_1 to the E_4 level by a CO_2 laser. They then quickly relax to the E_3 level by LO-phonon scattering. Similarly, the electrons on the E_2 level can be emptied quickly to E_1 through LO-phonon scattering. THz emission takes place between E_3 and E_2. [Q. Hu et. al., 1998]

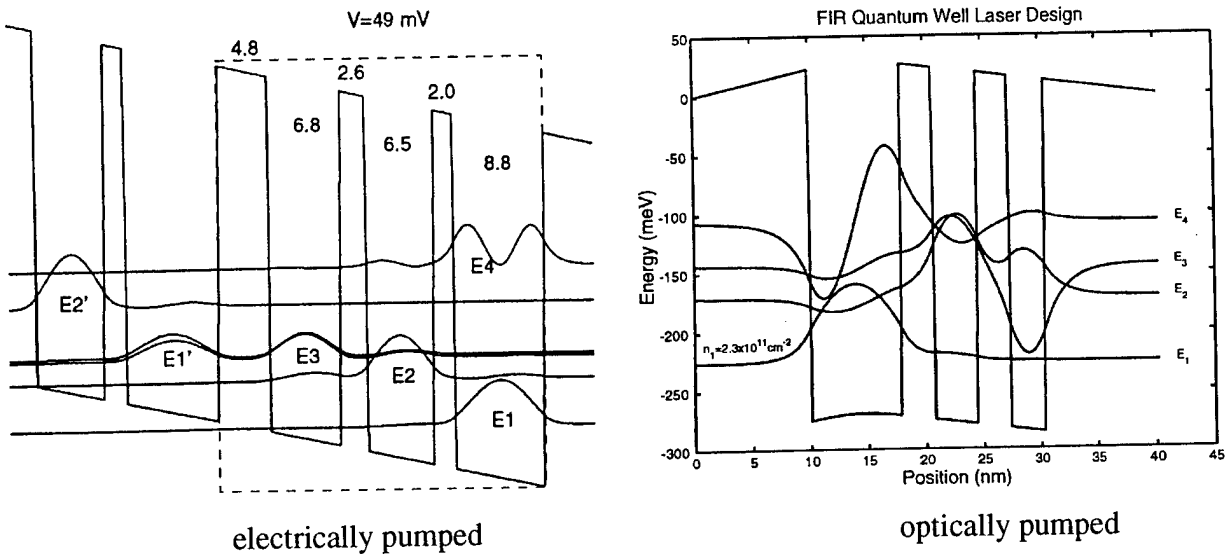

electrically pumped

optically pumped

Figure 1-3. Band profiles and squared wave functions for electrically and optically pumped THz emitters and detectors. [Q. Hu et al., 1998]

Quantum Cascade Lasers (QCLs)

The basic operation of the QCL is shown in Figure 1-4 (QCL). The basic idea is that many photons can be created by a single electron cascading through many quantum wells. A QCL is made by creating two regions of multiple quantum wells such that three energy levels exist. The quantum wells are "made" by growing a few atomic layers of different alloys with different band gaps. Some material systems used are InGaAs/InAlAs and GaAs/AlGaAs. The two regions are the injector and active regions. The energy levels are designed so that an electron transition of E_3 to E_2 generates photons of frequency $\nu = (E_3 - E_2)/h$, the residence time of electrons at E_2 are made small by designing E_1 to contribute to a scattering process such as LO phonon scattering which will greatly reduce the electron residence time at E_2 relative to E_3, and under bias the E_1 and E_3 energy levels allow efficient electron tunneling from one active region to the next via resonant tunneling in the injector region. The injector region is also designed to promote mode confinement. The design allows an electron to cascade through a set of stacked injector/active regions giving the possibility for one electron to generate many photons.

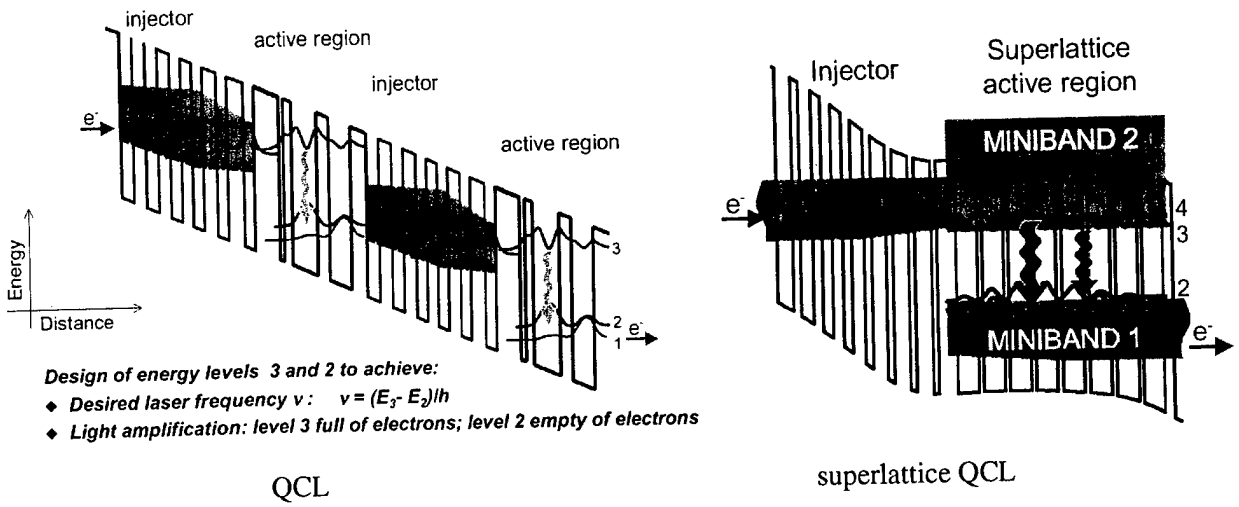

Figure 1-4. Conduction band profiles illustrating the operation and design of the Quantum Cascade Laser (QCL) and the superlattice QCL. [Faist et al., 1996], [Capasso et al., 1999]

Some of the attractive features of the QCL are that the operational wavelength can be designed into the THz region and is determined by the layer thickness rather than by material composition, so potentially all the mid infrared spectrum can be covered by the same material. Also, since each electron creates in principle N laser photons in traversing an N-stage cascaded structure (N = 20 - 75) the theoretical quantum efficiency is high making the device an intrinsically high power laser. Finally, due to its semiconductor construction, the QCL will potentially have a low failure rate, a long lifetime, and have low fabrication costs.

The QCL has made many milestones. Laser wavelengths from 3.4 to 17 μm have been shown. Pulsed mode peak optical powers of 0.5 W at room temperature and an optical power of 0.2 W at liquid-nitrogen temperature in continuous mode have been demonstrated. The optical signal has been shown to have high spectral purity enabling single mode lasing. Wide single-mode tuning has been demonstrated enabling high resolution spectroscopy. The gas sensing capability of grown QCLs has also been demonstrated. The flexibility of design of the QCL has also been shown with the superlattice QCL shown in Figure 1-4 which uses a superlattice to create "minibands" which set the electron energy of electron transition for photon production [Capasso, et. al., 1999].

Two major obstacles face quantum cascade laser designers to enable operation in the longer-wavelength THz range [Q. Hu et. al., 1998]. The first obstacle is that the narrow energy level requirements (1 THz = 4 meV) will push crystal growth technology, make the detection and analysis of spontaneous emission difficult, and increase the effect of heating and hot electron tunneling. The second obstacle is mode confinement. Mode confinement is difficult at longer wavelengths where conventional dielectric waveguide confinement is not applicable because the evanescent field penetration, proportional to the wavelength and on the order of several tens of microns, is much greater than the active gain medium of several microns.

Quantum Well Infrared Photodetectors (QWIPs)

A Quantum Well Infrared Photodetector (QWIP) uses intersubband transitions in multiple quantum wells to detect frequencies in the infrared. QWIPs operation is diagrammed in Figure 1-5. Infrared radiation incident on the MQWs photoexcite bound state electrons into the quasibound states and continuum states generating photocurrent which can be detected by a circuit. An alternative is to use small band gap materials and rely on valence band to conduction band excitation. Currently however low band gap materials are extremely difficult to grow.

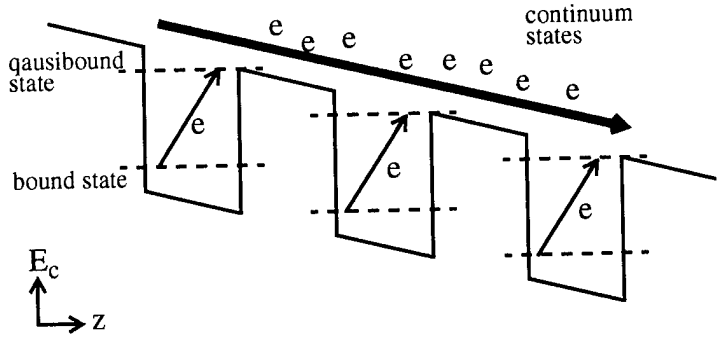

Figure 1-5. Conduction band diagram illustrating Quantum Well Infrared Photodetector (QWIP) operation.

By varying the thickness of the layered materials (such as GaAs/AlGaAs) a designer can tune the spectral responsivity of the QWIP. Improving the performance of the QWIP depends largely on minimizing the dark current (current flowing through the device when no photons are incident on the device). The three main sources of dark current in QWIPs are ground state tunneling, thermally assisted tunneling, and thermionic emission. Ground state tunneling between quantum wells depends on barrier height and widths, and dominates at lower temperatures (< 30 K). Thermally assisted tunneling of a thermally excited electron through the barrier tip into the continuum states dominates at medium temperatures. Thermionic emission dominates at high temperatures (bound state electrons thermally excited into the continuum states).

1.2 Importance of a Terahertz Quantum Device Design Tool

The development of solid state terahertz devices (0.3 THz - 10 THz) will enable the development of sources and detectors for use in atmospheric sensing, object detection, point to point communication, spectroscopy and biological detection. Many current THz device designs rely on multiple quantum wells designs with electrons making intersubband transitions. The THz device design must account for quantum effects such as quantum resonant modes, quantum mode mixing, tunneling, resonant tunneling, intersubband transitions, side wall scattering, and surface recombination. Currently, there are no CAD tools available that incorporate all the proper physics for designing THz quantum devices. Such a design tool could be used to lower research cycle time by minimizing empirically-driven device and circuit development.

Circuit designers use circuit simulators such as SPICE to design and analyze high speed circuits. In circuit simulators equivalent lumped elements characterize the actual device behavior. The equivalent lumped element parameters are typically extracted from the DC current-voltage curve

and the frequency dependent S-parameter curve. Both curves can be measured experimentally and include parasitic device effects. Computer modeling of individual devices should calculate these curves to provide understanding of the device performance and shed light on possible improvements that impact the overall circuit performance.

The quantum device simulation CAD tool discussed here can be used to lower quantum device research cycle time by minimizing empirically-driven device and circuit development, aid in formulating new device concepts, and help quantify the performance trade-offs when incorporating quantum devices into circuits.

1.3 Project Objectives

The overall objective of this effort is to develop a commercial quality, validated computer aided design (CAD) tool to aid in the development of THz quantum based semiconductor devices. The quantum CAD tool will be a device simulator with the ability to investigate the operation of and generate reduced models (S-parameters) for quantum based, electronic and photonic THz sources and detectors such as quantum cascade lasers, superlattices, and multiple quantum wells.

The approach to accomplish this objective is to modify and validate an existing quantum simulator NEMO:

a. couple to drift-diffusion and/or hydrodynamic models to enable multi-scale studies of semiconductor devices

b. further improve the small signal ac analysis to allow the study of THz devices

c. demonstrate and validate the quantum/classical model on several different quantum devices using published experimental results

d. integrate the tool into CFDRC's commercial CAD environment

The planned focus for phase II would be a more thorough solution of the electromagnetics problem using ϕ-A and FVTD formulations to solve for the varying fields in the quantum, lightly and heavily doped contact regions, and in the metal contacts where skin effects become important. Large ac signal analysis would be implemented into the simulator to enable s-parameter generation which will help device designers integrate the MQW solid state THz devices into a circuit. Rate equations for electron transitions would be solved. Equations for photon creation and transport would be solved. Complex mobilities would be incorporated into the contact regions to address high frequency effects of electron transport when the driving frequency exceeds the scattering rate. The energy equation would be solved for to determine heating effects on device performance.

2.0 NEMO

An existing quantum simulator, the NanoElectric MOdeler (NEMO) [Blanks et al., 1997], is being used to solve the Schrödinger wave equation and Poisson's equation. An overview of NEMO will be given followed by a more detailed description of the calculations carried out in NEMO.

NEMO was developed under government funding by Raytheon / TI for the quantitative analysis of resonant tunneling diodes. NEMO is presently the only quantum device design and analysis code that can predict and analyze the performance of realistically extended tunneling structures including the effects of contacts, scattering, and bandstructure. For instance, NEMO is the first quantum device design tool that has proven to be quantitatively predictive in the DC current-voltage simulation of real world high performance resonant tunneling diodes. The generality and comprehensiveness of NEMO stem from the non-equilibrium Green's function (NEGF) theoretical approach. This formalism enables the inclusion of the essential semiconductor electron transport physics such as open systems, realistic bandstructure models, charging, and scattering. Other methods such as the Schrödinger wave equation, Density Matrix, or Wigner function approaches are simplifications of and can be derived from the more general NEGF approach. These other approaches have promised to simulate the full time-dependent electron transport dynamics in RTDs. However, in more than 15 years of research these approaches have not been able to quantitatively predict the simple DC current voltage characteristic of a suite of real world RTDs. NEMO, which is based on NEGF, is the first simulator to have done so. NEMO was originally limited to the simulation of DC current voltage characteristics. Recent modifications by CFDRC have also allowed NEMO to carry out small signal AC analysis.

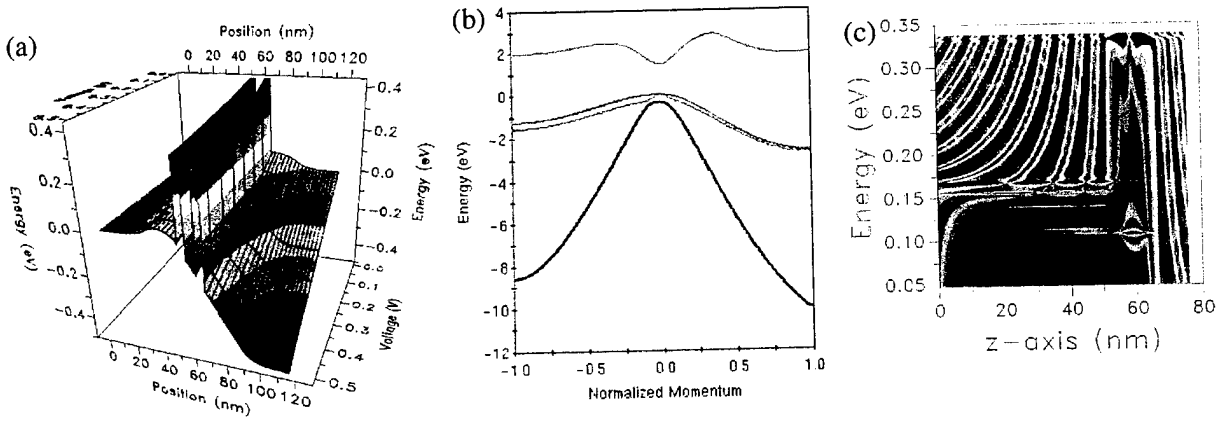

Figure 2-1. NEMO example calculations of (a) band profile as a function of energy and position, (b) 10- band, band structure for AlGaAs, and (c) density of states for a 2-barrier RTD device as a function of energy and position

The NanoElectric MOdeling (NEMO) program is the result of a three year development effort involving four universities and the corporate research lab of Raytheon (formerly Texas Instruments). The program is a quantum device modeling tool for layered semiconductor structures. NEMO can model one-dimensional two-terminal heterostructure devices. Some example calculations are shown in Figure 2-1. NEMO calculates 10 main quantities:

- I-V curves (current through the device as a function of the voltage applied across the device)
- carrier density, n(z)
- spectral distribution (or density of states) A(E,k,z) as a function of particle energy E, momentum k, and position z
- transmission coefficient of carriers through layered heterostructure, T(E,k)
- current density of carriers, J(E,k)
- energy of the carriers, E(k)
- resonance list, specifically the complex poles (eigenvalues) of $(E - H_0 - \Sigma^R - \Sigma^{RB})^{-1}$ where H_0 is the bare Hamiltonian, Σ^R is the self energy resulting from scattering, and Σ^{RB} accounts for the open system boundaries.
- resonant wave functions corresponding to resonance list (eigenfunctions)
- band structure, specifically the band edges at Γ and X (points in the brillouin zone which correspond to direct and indirect bands) as a function of energy and momentum
- AC analysis as the admittance of the system ($\mathbf{I/V} = \mathbf{Y} = G + jB$)

NEMO includes the effects of quantum charging, bandstructure and incoherent scattering from alloy disorder, interface roughness, ionized dopants, acoustic phonons, and polar optical phonons. The Schrödinger time independent wave equation solution is based on the non-equilibrium Green's function formalism [Lake et al., 1997]. Band structure can be included in four different models: 1-band tight binding, 2-band k-p, nearest-neighbor sp3s*, and 2nd nearest neighbor sp3s*. The self energies resulting from static disorder or phonons can be calculated to any finite order or to infinite order in the self-consistent Born approximation. Charging can be calculated semi-classically (Thomas-Fermi) or quantum mechanically (Hartree).

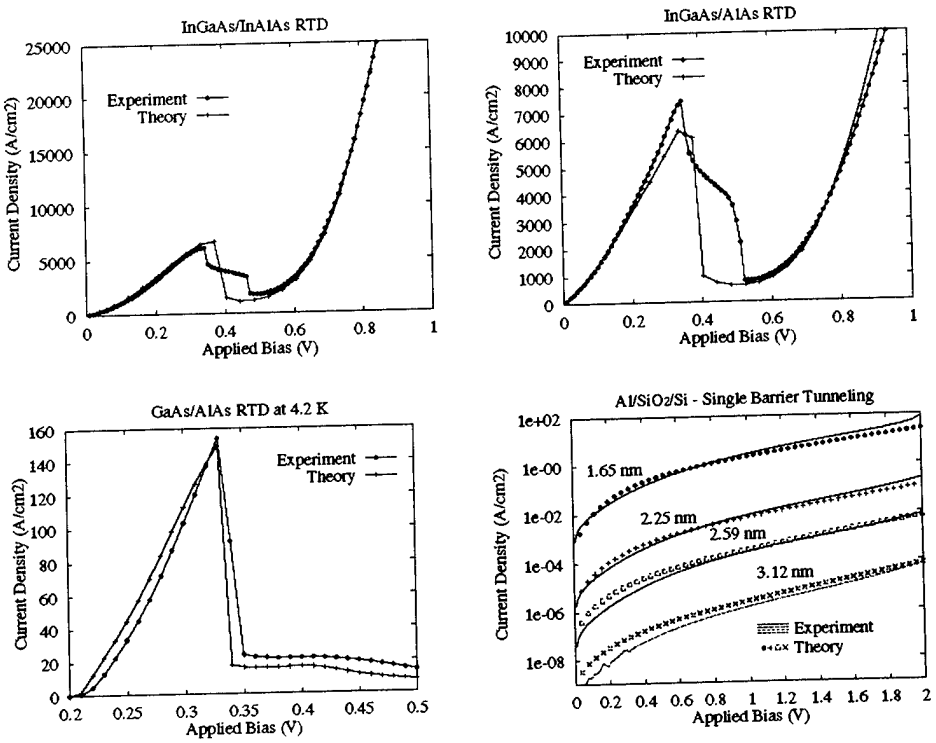

Figure 2-2. I-V simulations for four different classes of tunneling devices obtained using NEMO in previous work. The simulations are compared to experimental data. (a) InGaAs/InAlAs lattice-matched RTD at room temperature. Simulation is based on a full-band, quantum-charge self-consistent sp 3 s* model without scattering. (b) High performance InGaAs/AlAs pseudomorphic strained RTD at room temperature. Simulation model is the same as in (a). (c) GaAs/AlAs RTD at 4.2 K showing a scattering-assisted valley current (phonon peak). The single-band simulation includes scattering caused by polar optical phonons, interface roughness, and acoustic phonons. Band structure effects can be ignored in this device at low T. (d) $Si/SiO_2/Al$ single-barrier structure. Simulation is based on single-band model.

The non-equilibrium Green's function formalism provides a method for calculating the non-equilibrium statistical ensemble average of the single particle correlation operators. The open boundary conditions model large regions of the contacts as collector and emitter reservoirs even when there are spatially varying potentials in the regions. The boundary conditions allow modeling long devices where only a small region requires a more rigorous quantum mechanical treatment such as the inclusion of scattering. The boundary conditions are also capable of injecting electrons into the device from mixed, non-asymptotic states in the emitter. Interface roughness is modeled as a layer of alloy in which the cation species of a given type cluster into islands. Interface roughness self-energies are calculated for both Gaussian and exponential autocorrelation models.

NEMO incorporates the important physics of band structure, charging, and incoherent scattering for a wide variety of materials as demonstrated in Figure 2-2. Self-consistent quantum charging and accurate band structure are essential for modeling the high-performance In-based RTDs shown in Figure 2-2(a) and Figure 2-2(b). The band structure must be calculated for bulk materials and

also for the strained, pseudomorphic materials used in the best RTDs, as illustrated in Figure 2-2(b). For the very best RTDs [Moise et al., 1995], one must also include incoherent scattering to quantitatively predict the valley current. Presently, NEMO includes incoherent scattering within a single-band model, as shown in Figure 2-2(c) for a GaAs/AlAs RTD at 4.2 K. NEMO is not limited to III-V compounds. Figure 2-2(d) shows the tunneling current through an $Al/SiO_2/Si$ structure for various SiO_2 thickness. More examples of NEMO calculations are presented at the NEMO web site located at www.cfdrc.com/nemo.

Emitter, Quantum, and Collector Regions

NEMO separates a quantum device into three regions: the emitter reservoir, the quantum region and the collector reservoir. The reservoirs are treated semi-classically, assumed to be in thermal equilibrium, and act as a source (or sink) of charge carriers. The distribution of these carriers in allowed energy states of the emitter reservoir serve as a source of carriers at each energy. The second region is the quantum region and is made up of some type of barrier/well combination. Semiclassically, no carriers are allowed to traverse the barriers unless they have energies greater than the height of the barriers. So, the quantum region is treated quantum mechanically by solving the one-dimensional time-independent Schrödinger wave equation from which, among other things, the transmission coefficient in the quantum region as a function of energy can be calculated. The third region is the collector. It is treated the same way as the emitter, except that the distribution of unoccupied energy states are calculated. These are the energy states which carriers may flow into when exiting the device region.

For current to flow, there must be free carriers available in the emitter at energies at which the transmission of the device region is greater than zero and there must be unoccupied energy states in the collector. Or, more succinctly stated:

$$J(E,k) = T(E,k)[f_{Em}(E) - f_C(E)] \tag{2.1}$$

where E is the energy of the carriers, k is the transverse momentum of the carriers, J(E,k) is the carrier current density at energy E and transverse momentum k, T(E,k) is the transmission coefficient of the quantum heterostructure, and $f_{Em}(E)$ and $f_C(E)$ are the probability of a carrier (i.e., electron or hole) occupying an energy state E in the emitter (Em) or collector (C) regions of the device respectively. Described above is the main calculation that NEMO does. In the process of this calculation, it also calculates many intermediate quantities, such as density of states (also called spectral function), resonances of the device region, etc.

In the emitter (collector) the available (unoccupied) carrier density at each energy level n(E) is calculated from

$$n(E) = DOS(E)\frac{1}{1 + e^{(E - E_f)/(kT)}} \tag{2.2}$$

and depends upon the temperature T of the bulk material and the density of states (DOS). Temperature effects the thermal equilibrium occupation and the band structure, E(k). Given the

DOS and T one can calculate the Fermi level in the reservoirs. For the DOS, a parabolic E(k) relationship can be assumed or it can be calculated numerically from the Hamiltonian where the band structure model selected for the device is used. Inelastic scattering in the emitter and collector is also accounted for by letting carriers occupy quasi-bound states in the reservoirs that will exist when band bending causes there to be a small notch just beside the first barrier. The lifetime of particles in these states can be specified as either exponential decay, Lorentzian decay, or energy independent.

Electric Potential of the Device

When a bias is applied to the device, the free carriers will redistribute themselves until they reach equilibrium. This will cause a change in the electric potential $\phi(z)$ across the device. In order to take this effect into account, the charge and potential are calculated self consistently, according to the user specified potential model (Hartree or Thomas-Fermi). The electrostatic potential is calculated using Poisson's equation:

$$\nabla \bullet \varepsilon_r \nabla \phi = -\frac{q}{\varepsilon_0}[N_{D_i} - n_i(\phi)] \tag{2.3}$$

where q is the electron charge, N_{Di} and n_i and are the donor concentration and free electron density respectively at layer i, and e is the electric permittivity. In the reservoirs $n_i \propto f_i\ DOS(E)_i$ where f_i is the Fermi-Dirac distribution function for layer i. In the quantum region $n_i \propto G^<_{i,i}$ for the Hartree potential and $n_i = 0$ for the Thomas-Fermi potential. In the reservoirs, the $DOS(E)_i$ is calculated taking ϕ_i into account. In the quantum region, the n_i is calculated quantum mechanically. The n and ϕ parameters are calculated iteratively until convergence is achieved.

Calculation and Integration of Green's Function

In the quantum region of the device NEMO solves, among other things, the one-dimensional time-independent Schrödinger wave equation. The general form of the Hamiltonian used is

$$H = H_0 + H_{pop} + H_{ac} + H_{ir} + H_{al} + H_{id} \tag{2.4}$$

where H_0 contains the kinetic energy and the effects of the band structure, the applied potential, and the Hartree potential. The five terms to the right represent the potential felt by the electrons due to polar optical phonons, acoustic phonons, interface roughness, alloy disorder, and ionized dopants respectively.

H_0 is broken down into five terms which are the Hamiltonian of the quantum region, the left contact, the right contact, the coupling of the left contact to the quantum region, and the coupling of the right contact to the quantum region.

$$H_0 = H_0^D + H_0^L + H_0^R + H_0^{LD} + H_0^{RD} \tag{2.5}$$

One method of solving Schrödinger equation is to find the Green's function, which satisfies the equation:

$$[H(k) - E]G(k,E) = \delta(r - r') \tag{2.6}$$

$$\text{so } G(k,E) = [H(k) - E]^{-1} \tag{2.7}$$

NEMO uses the non-equilibrium Green's function approach to perform an ensemble average over the free charge carriers in the device. The density of states, transmission coefficients, current, etc., all fall out of the calculation of the correlation Green's function, $G^<(k,E)$. In general, there is a $G^<_{i,j}$ for every layer i and j in the device region, and it is an mxm matrix where m is the number of bands in the model used.

G is a function of longitudinal energy, E, and transverse crystal momentum, k. Any observable (current or charge, for example) calculated with G, must be integrated over E and k. For example, the current at layer i

$$J_i \alpha \int\int dE dk T(k, E)[f_L(E) - f_R(E)] \tag{2.8}$$

where T(k,E) is the transmission coefficient, calculated with $G^<$, and $f_{L(R)}$ is the thermal equilibrium fermi factor in the emitter (left lead) and collector (right lead).

One of the band models available in NEMO is a parameterized single band model that mimics the E(k) dispersion relation found using a more complicated model. This is a more efficient way of treating a device that exhibits strong non-parabolicity in the conduction band, but in which current flows mainly in the conduction band. In this situation, it is essential to use a multiband model in order to correctly reproduce the structure of the conduction band, but not essential to account for current flowing in more than one band because significant current does not flow in any other band. Consequently, NEMO uses a parametrized version of the single band effective mass Σ's equation. To do this, it must first find the structure of the band, then the hopping elements and site energies are parameterized as functions of E and k.

3.0 DRIFT DIFFUSION TRANSPORT FOR CARRIERS IN TERMINAL REGIONS OF NEMO

One of the objectives of this project is to include better physical transport models in the collector and emitter terminal regions in NEMO. Before the development, NEMO modeled the emitter and collector terminals as a reservoir of carriers in thermal equilibrium with the lattice. This was implemented by enforcing a flat band condition (flat fermi level) in the terminal regions. This approximation works well for degenerately doped semiconductors. However, for thin or moderately doped contacts this approximation begins to breakdown. In this project NEMO underwent development to demonstrate electron transport using a drift-diffusion formulation instead of assuming a thermalized sea of electrons. This has improved the carrier transport mechanism in the terminal regions.

The basic equations for the drift-diffusion model [Sze, 1981] are Poisson's equation and the current continuity equations for electrons and holes take the following traditional form

$$\nabla \bullet \varepsilon_r \nabla \phi = -\frac{\rho}{\varepsilon_o} \tag{3.1}$$

$$\frac{\partial c_\alpha}{\partial t} = G_\alpha - U_\alpha + (-1)^{\alpha+1} \nabla \bullet [\mu_\alpha c_\alpha \mathbf{E} + (-1)^{\alpha+1} D_\alpha \nabla c_\alpha] \tag{3.2}$$

where $\alpha = 1$ or 2 denotes the equation for electrons or holes respectively, c_α is the particle number density, G_α is the particle generation rate, U_α is the particle recombination rate, μ_α is the particle mobility, D_α is the particle diffusion coefficient, ϕ is the electric potential, ε_r is the electric relative permittivity, ε_o is the permittivity of free space, and ρ is the space charge due to electrons, holes, or traps. From the electric potential the electric field $\mathbf{E}$ is calculated ($\mathbf{E} = -\nabla\phi$). The generation (G) and recombination (U) terms can include phenomena such as impact ionization, photon generation of carriers, or spontaneous and stimulated emission [Li, 1997].

The drift-diffusion formulation can be used for the bulk region, where the material composition changes slowly. Poisson's equation is already solved for in NEMO. However, modifications must be made for materials with position-dependent band structure [Grupen, 1991]. Also, at an abrupt heterojunction interface the thermionic emission process [Hess, 1988] and tunneling across the heterointerface [Zeeb, 1992] must be taken into account. Both thermionic emission and tunneling at the heterointerface can be taken into account as a thermionic-field boundary condition at the abrupt heterojunction [Yang, 1993].

Since NEMO uses a Green's function approach for tunneling and quantum charging a different approach was taken when solving the drift-diffusion equations. The approach uses the total carrier density and current density due to all effects, quantum and classical, to determine the variation of the fermi level in the terminals (previously these were set to a constant value). The details of its implementation follows. First, there is a discussion of boltzmann transport where the expression solved in the terminal regions is derived. Next is a discussion of the numerical implementation of drift diffusion in the terminal regions of NEMO.

3.1 Boltzmann Transport and Drift Diffusion

The distribution function f can be constructed based on the quasi-thermal equilibrium distribution function f_0 using perturbation theory [R. Stratton, 1972]

$$f(\mathbf{r}, \mathbf{k}) = f_0(\mathbf{r}, \mathbf{k}) - \tau(\mathbf{r}, \mathbf{k})\left[\frac{h}{2\pi m^*}\mathbf{k}\nabla f_0 - \frac{h}{2\pi m^*}\frac{\partial f_0}{\partial \mathcal{E}}\mathbf{k} \bullet \mathbf{E}\right] \tag{3.3}$$

where **r** is the position vector, **k** is the wave number vector, τ is the relaxation time and depends on position and wave number, **E** is the electric field, m^* is the effective mass, and $\mathcal{E}$ is the carrier kinetic energy. For electrons the carrier kinetic energy is $\mathcal{E} = E - E_C$, where E is the total carrier energy and E_C is the conduction band edge.

Once the distribution function f is known the current density can be determined. For electrons the current density is

$$\mathbf{J}_n = -q\int \mathbf{v} f(\mathbf{r}, \mathbf{k})\frac{1}{(2\pi)^3}dk_x dk_y dk_z \tag{3.4}$$

where **v** is the carrier velocity.

Eq. 3.3 and Eq. 3.4 can be simplified by making some assumptions. One is to assume the effective mass m^* is constant for a parabolic band structure in which case the carrier velocity **v** and wave number **k** are related by $\mathbf{v} = h\mathbf{k} / 2\pi m^*$. Second is to assume the relaxation time τ can be simplified to depend on position **r** and kinetic energy $\mathcal{E}$ (i.e., $\tau(\mathbf{r},\mathbf{k}) = (\mathbf{r},\mathcal{E})$). With these assumptions Eq 3.3 and Eq 3.4 can be simplified to

$$f(\mathbf{r}, \mathbf{v}) = f_0(\mathbf{r}, \mathbf{v}) - \tau(\mathbf{r}, \mathcal{E})\left[\mathbf{v} \bullet \nabla f_0 - q\frac{\partial f_0}{\partial \mathcal{E}}\mathbf{v} \bullet \mathbf{E}_n\right] \tag{3.5}$$

$$\mathbf{J}_n = q\int \tau(\mathbf{r}, \mathcal{E})\mathbf{v}\mathbf{v} \bullet \nabla f_0 d^3v - q^2\left(\int \tau(\mathbf{r}, \mathcal{E})\frac{\partial f_0}{\partial \mathcal{E}}\mathbf{v}\mathbf{v}d^3v\right) \bullet \mathbf{E}_n \tag{3.6}$$

where $\mathbf{E}_n = \nabla E_C/q$, the kinetic energy $\mathcal{E} = m^*\mathbf{v}^2/2$, and the expressions are for electrons.

Assume the quasi-thermal equilibrium distribution function f_0 takes the form of Fermi-Dirac statistics given by

$$f_0(\mathbf{r},\mathbf{k}) = \frac{2}{1+\exp\left(\dfrac{\mathcal{E}(\mathbf{k})+E_C(\mathbf{r})-E_{Fn}(\mathbf{r})}{k_B T_n}\right)} \tag{3.7}$$

Taking the gradient of the quasi-thermal equilibrium distribution function f_0

$$\nabla f_0(\mathbf{r},\mathbf{k}) = \frac{\partial f_0}{\partial \mathcal{E}}\left(\nabla E_C - \nabla E_{Fn} - \frac{\mathcal{E}(\mathbf{k})+E_C(\mathbf{r})-E_{Fn}(\mathbf{r})}{T_n}\nabla T_n\right) \tag{3.8}$$

and plugging into the simplified current density expression (Eq. 3.6) yields

$$\mathbf{J}_n = n\mu_n \nabla E_{Fn} + qn\left[D_n^T + \frac{k_B}{q}\left(\frac{3}{2}\frac{F_{1/2}(\eta_n)}{F_{-1/2}(\eta_n)} - \eta_n\right)\mu_n\right]\nabla T_n \tag{3.9}$$

where n is the electron number density, μ_n is the electron mobility, D_n^T is the thermal diffusivity for electrons, $F_{1/2}$ and $F_{-1/2}$ are fermi integrals, and Planck's constant $\eta_n = (E_{Fn} - E_C)/k_B T_n$. The electron mobility μ_n is given by

$$\mu_n = -q\frac{1}{n}\frac{8\pi}{3h^3}\sqrt{2m_n^*}\int \tau(\mathbf{r},\mathcal{E})\frac{\partial f_0}{\partial \mathcal{E}}\mathcal{E}^{3/2}\,d\mathcal{E} \tag{3.10}$$

Assuming there are no temperature gradients throughout the device Eq. 3.9 reduces to

$$\mathbf{J}_n = n\mu_n \nabla E_{Fn} \tag{3.11}$$

This is the expression which is solved in the contact regions of the NEMO simulator. The change in the fermi level through the terminals is determined from the known current density and carrier density.

3.2 Numerical Implementation

The NEMO solver divides the heterostructure device into different simulation domains as shown in Figure 3-1. The terminal regions define where the Fermi levels are flat and the free carriers are calculated semi-classically. The quantum region is where the wave function is solved using the Green's function formalism. Within the quantum region there are the non-equilibrium, quantum charge, and resonance finding regions. In the non-equilibrium region transport and scattering can be calculated. The quantum region which is not a part of the non-equilibrium region is treated as a reservoir with a characteristic relaxation rate. The quantum charge region is where charge is calculated quantum mechanically. Outside this region charge is taken from a semi-classical solution. The quantum charge region is larger than the non-equilibrium region. The resonance finding region is the region of space where eigen-state maxima must appear in order to be accepted as bound states.

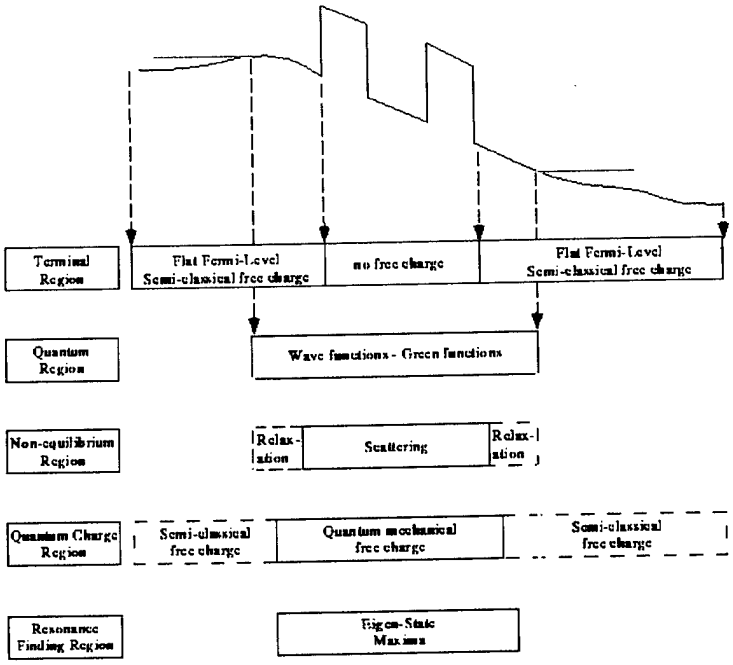

Figure 3-1. Conduction band edge of a layered heterostructure and simulations domains in NEMO.

The model used is To try and get a i-v curve a problem was set-up where quantum transport by resonant tunneling is calculated in the center quantum well in the superlattice and the other quantum wells are modeled as equilibrated fermi baths of carriers with a characteristic relaxation time.

The reservoir relaxation model used in the terminal region where quantum quantities are calculated is as follows. Electrons can be sourced out of emitter quasi bound states in a NEMO I-V simulation. These emitter quasi bound states are not directly coupled to the flat-band state continuum. To serve as carrier sources these states have to be given a finite scattering life-time due to inscattering of carriers from higher states in the reservoir. The current is proportional to the rate of filling of these emitter quasi bound states. The relaxation rate enters the Hamiltonian in the leads as an optical potential $\sigma = h/4\pi\tau$ above the conduction band edge. For the treatment of $\sigma(z,E)$ below the conduction band an exponentially damped relaxation is used given by

$$\sigma(z, E) = \sigma_0 e^{\frac{E - E_c(z)}{\delta}} \tag{3.12}$$

where z is the spatial coordinate, E is energy, EC is the conduction band edge as a function of position, δ is a damping factor, and σ_0 is an optical potential ($h/4\pi\tau$).

The terminal regions are where Eq. 3-11 is used. In the previous formulation the fermi level is constant across the terminal regions although the conduction and valence band edges are allowed to bend. With the new formulation the fermi level is now a function of position. The fermi level relative to the conduction band is fixed at the emitter and collector boundaries. The variation through the terminal region is then calculated using a discretized form of Eq 3-11 given by

$$E_{Fn}^{k+1} - E_{Fn}^{k} = \frac{J_n}{n\mu_n}(z^{k+1} - z^{k}) \tag{3.13}$$

where the index k delineates mesh points on the grid, and z is a spatial position on the grid.

Currently, this calculation is done only for electrons and with no generation/recombination mechanisms. This option is integrated into the GUI. A snapshot of the GUI with this option highlighted is shown in Figure 3-2.

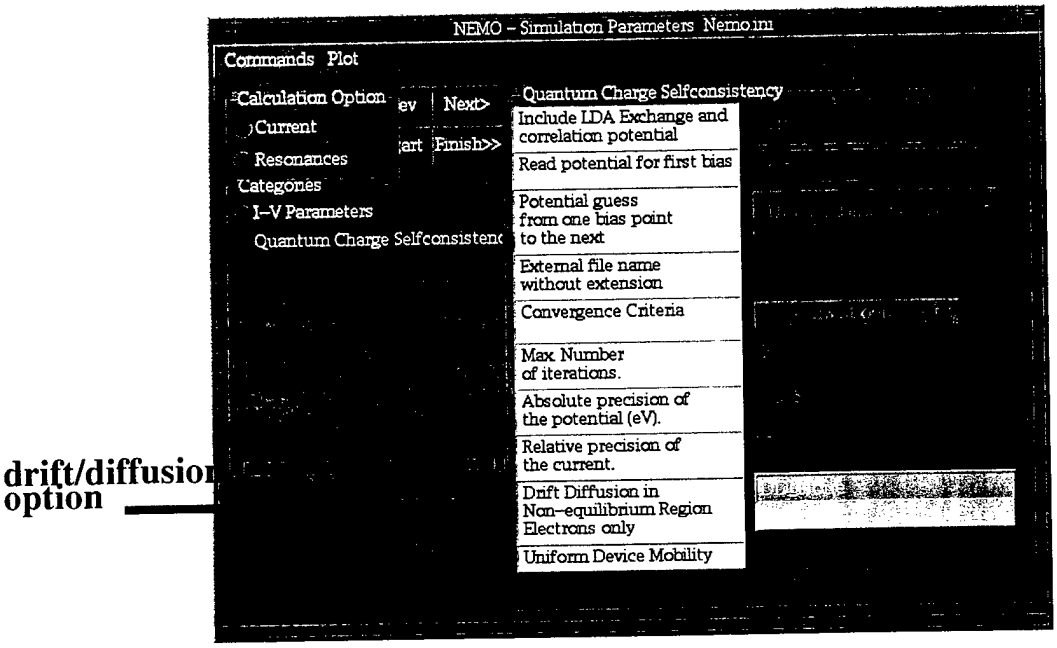

Figure 3-2. NEMO GUI showing location of option to solve for a simple drift/diffusion formulation in the terminal regions.

4.0 SMALL SIGNAL AC ANALYSIS

Small signal AC analysis is implemented in NEMO via a linear perturbative approach described by Fernando and Frensley [Fernando and Frensley, 1995]. A small sinusoidal potential is added to the diagonal of the Hamiltonian resulting in the generation of harmonics. Each harmonic corresponds to the order of response of the system due to the perturbing potential. The electric current resulting from the first and second order harmonics can be expressed as follows:

$$I = I_0 + \frac{v}{2}(ye^{i\omega t} + y^* e^{-i\omega t}) + \frac{a_{rect}v^2}{4} + \frac{v^2}{8}(a_{2\omega}e^{2i\omega t} + a_{2\omega}^* e^{-2i\omega t}) \tag{4.1}$$

Here, I_0 is the DC current, v is the amplitude of the sinusoidal perturbation, y is the AC admittance, a_{rect} is the 2nd order rectification coefficient, and $a_{2\omega}$ is the 2nd order generation coefficient. The simulation of N orders of response requires the solution of N coupled Hamiltonians.

An AC potential is included in the Hamiltonian by adding the matrix elements of a sinusoidal perturbation. These matrix elements result in the generation of harmonics whose first order coefficients provide AC conductance and susceptance. The matrix elements of the DC Hamiltonian in NEMO is represented as follows,

$$\langle \alpha, L, k | H^{DC} | \alpha', L', k' \rangle = D^{DC}_{\alpha,\alpha'}(k)\delta_{L,L'} - t^{DC}_{\alpha,L;\alpha',L'}(k)\delta_{L',L\pm j\neq 0} \tag{4.2}$$

The submatrices D^{DC} and t^{DC} are of the order of the basis of the bandstructure model. The diagonal block contains the on-site orbital energies and the electrostatic potential while the off diagonal block contains site to site interaction energies. The addition of an AC perturbation results in coupled harmonic sidebands. The AC Hamiltonian including only the first order harmonics may be expressed as follows:

$$D^{AC} = \begin{bmatrix} D^{DC} - \frac{h\omega}{2\pi}\frac{v^{AC}}{2}I & \cdots \\ \cdots & D^{DC} + \frac{h\omega}{2\pi}\frac{v^{AC}}{2}I \end{bmatrix}, \quad t^{AC} = \begin{bmatrix} t^{DC} & \cdots & \cdots \\ \cdots & t^{DC} & \cdots \\ \cdots & \cdots & t^{DC} \end{bmatrix} \tag{4.3}$$

where ω is the frequency and v^{AC} is the magnitude of the perturbation. In NEMO all physical observables are calculated using the retarded Green's function. The retarded Green's function for a three monolayer device takes the following mathematical form.

$$G^R = \begin{bmatrix} E - D_1^{AC} - \Sigma_{1,1}^{RB} & t_{1,2}^{AC} & \cdots \\ t_{2,1}^{AC} & E - D_2^{AC} & t_{2,3}^{AC} \\ \cdots & t_{3,2}^{AC} & E - D_3^{AC} - \Sigma_{3,3}^{RB} \end{bmatrix} \tag{4.4}$$

The boundary self-energies, Σ^{RB}, couple electrons within the device to contact reservoirs assumed to be in thermal equilibrium. For the AC case the boundary self-energies take the form,

$$G^R = \begin{bmatrix} t_{0,1}^{DC} & \cdots & \cdots \\ \cdots & t_{0,1}^{DC} & \cdots \\ \cdots & \cdots & t_{0,1}^{DC} \end{bmatrix} \begin{bmatrix} J_0' \chi_{-h\nu} Z_{-h\nu} \chi_{-h\nu}^{-1} & J_{-1}' \chi_{-h\nu} Z_{-h\nu} \chi_{-h\nu}^{-1} & J_{-2}' \chi_{-h\nu} Z_{-h\nu} \chi_{-h\nu}^{-1} \\ J_1' \chi_0 Z_0 \chi_0^{-1} & J_0' \chi_0 Z_0 \chi_0^{-1} & J_{-1}' \chi_0 Z_0 \chi_0^{-1} \\ J_2' \chi_{h\nu} Z_{h\nu} \chi_{h\nu}^{-1} & J_1' \chi_{h\nu} Z_{h\nu} \chi_{h\nu}^{-1} & J_0' \chi_{h\nu} Z_{h\nu} \chi_{h\nu}^{-1} \end{bmatrix} - \tag{4.5}$$

$$J_m' = J_m \frac{v^{AC} 2\pi}{h\omega} \tag{4.6}$$

where J_m is the Bessel function of the first kind. The matrix $Z_{\Delta E}$ is a diagonal matrix of Bloch propagation factors for the bulk DC Hamiltonian shifted by energy ΔE. The columns of the matrix $\chi_{\Delta E}$ contain the corresponding Bloch eigenvectors.

5. COMMERCIAL CAD ENVIRONMENT INTEGRATION: CONVERTING GUI TO FOX

The process has begun to integrate NEMO into CFDRCs CAD environment. The first issue is updating the Graphical User Interface (GUI). The old GUI uses Motif and third party Motif widget sets (xrt-pdf) for plotting and table routines. Also, many parts of the GUI motif code were automatically generated using a GUI builder. The machine generated motif code that the GUI builder creates is very difficult to read, develop, and be further supported by humans. The GUI builder locks one into using the builder. Also, the Motif based code and 3rd party widget set cannot be ported easily to Windows (95/98/NT) machines. The GUI is being transitioned to the use of FOX libraries which are open source libraries (Free Objects for X, www.cfdrc.com/FOX/fox.html). This will allow a cross-platform GUI design from a single source, no reliance on a mixture of third party tools for GUI stability, and allow tighter integration with other CFDRC software. FOX is a C++ based tool kit for quickly developing fast, low memory, platform independent GUIs.

As a first step the FOX library will be used to replicate the functionality of the old GUI. In future releases the GUI will be enhanced and reorganized. Snapshots of the new GUI are shown in Figure 5-1. The main i-v calculation window, device window, and parameter list are completed. The database explorer, the material parameter list, and the band structure portions of the GUI shown in Figure 5-2 are near completion.

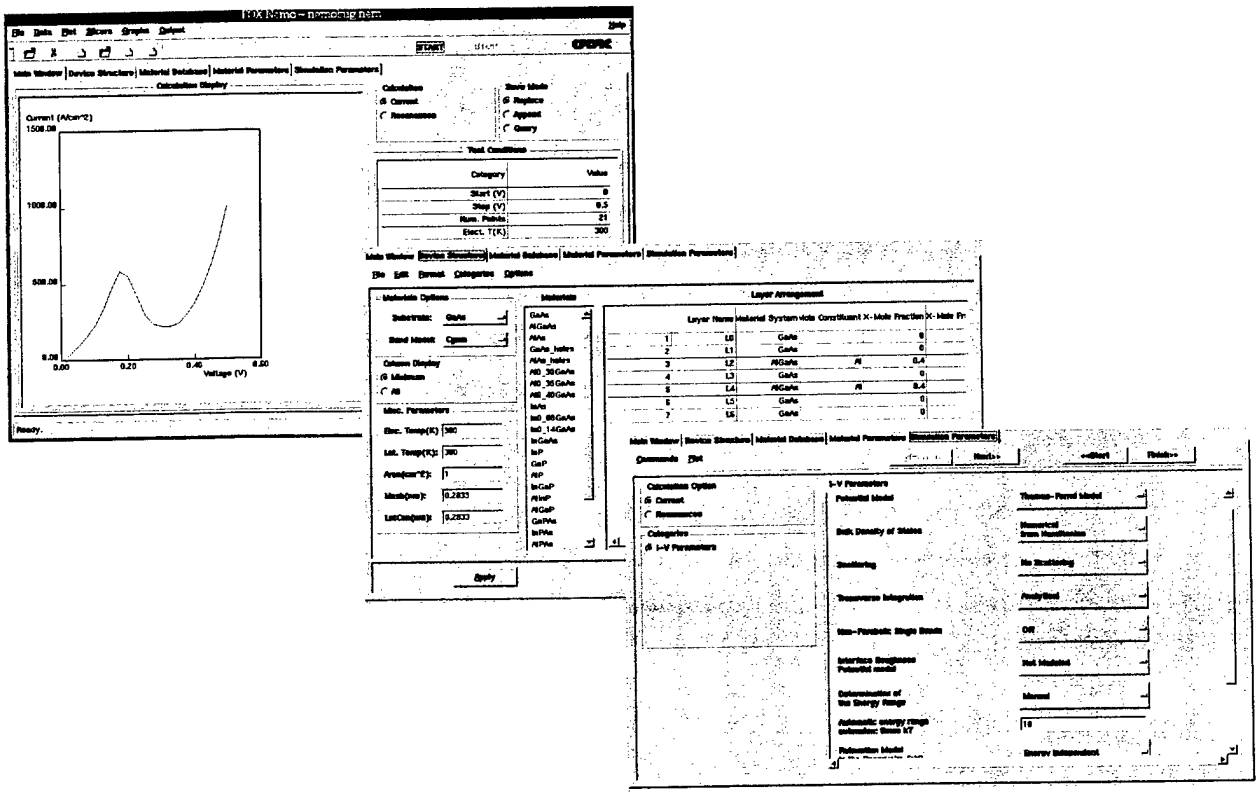

Figure 5-1. NEMO GUI using FOX libraries. Shown from left to right are the main window with an i-v calculation. The "device" window, and the "parameters" window.

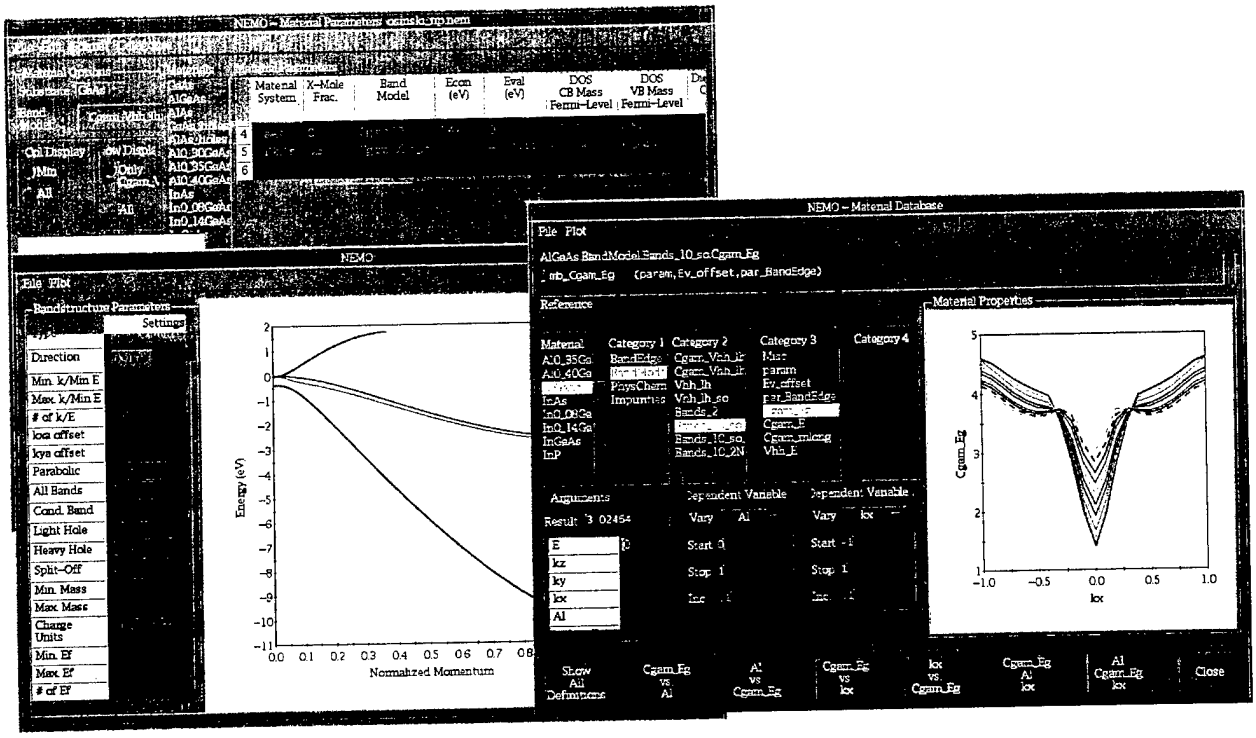

Figure 5-2. Parts of old NEMO GUI using Motif and 3rd party libraries. Shown are the material parameter, material database explorer, and bandstructure windows.

6.0 RTD STUDY

A resonant tunneling diode (RTD) device is used to demonstrate the drift-diffusion capability put into the contact regions of NEMO (Chapter 3) The resonant tunneling diode geometry which was simulated is shown in Figure 6-1. The ML unit used here is half the lattice constant of GaAs (0.2833 nm). The layer thickness (t) variation is assumed to be in the [111] lattice direction. All doping levels cited are donor number densities (N_D).

	N_D (cm^{-3})	t (nm)	t (ML)	comments
GaAs	1×10^{18}	30.03	106	nemo "collector"
GaAs	2×10^{15}	20.11	71	
$Al_{0.4}Ga_{0.6}As$	2×10^{15}	4.53	16	
GaAs	2×10^{15}	6.23	22	
$Al_{0.4}Ga_{0.6}As$	2×10^{15}	4.53	16	
GaAs	2×10^{15}	20.11	71	
GaAs	1×10^{18}	30.03	106	nemo "emitter"

Figure 6-1. Layer sequence of simulated resonant tunneling diode.

Solving drift-diffusion in the terminals will allow the terminals to drop part of the total voltage applied to the device. The doping in the terminals ($N_t = 10^{18}, 10^{16}$ cm^{-3}) and the electron mobility ($\mu = 10^3, 10^2$ $cm^2/V\text{-}s$) were varied. The electron mobility will only have an effect for the drift-diffusion cases. Plots of the conduction band edge, fermi level, electron density, and doping density are shown in Figure 6-2 with terminal doping and mobility varied. For instance the first two plots from the top correspond to $N_t = 10^{18}$ cm^{-3}, $\mu = 10^3$ $cm^2/V\text{-}s$, and a 0.5 V bias across the heterostructure with and without drift-diffusion calculated in the terminals. The case with drift-diffusion is marked. Without drift-diffusion (DD) the fermi levels remain flat, with DD the fermi level is seen to slowly vary with position near the collector terminal. The varying fermi-levels near the collector has an impact on the carrier concentration (slightly increasing the carrier level).

To explore when drift-diffusion will have more of an impact on device performance the doping density in the terminals was decreased and the mobility in the terminals was decreased. Both decreasing mobility and terminal doping density increase the effect of DD in the terminals. This can be seen in Figure 6-2. All cases show the applied voltage at which the fermi level begins to deviate from the flat band approximation. For high doping and mobility this is around 0.5 V. When the terminal doping is increased the applied voltage were an effect is seen is around 0.325 V. When the mobility is reduced the effect is seen to begin at around 0.45 V.

It should be emphasized that this is just a feasibility study. Much work needs to be done to improve the solver convergence. Holes, as well as generation and recombination effects, need to be included in the formulation.

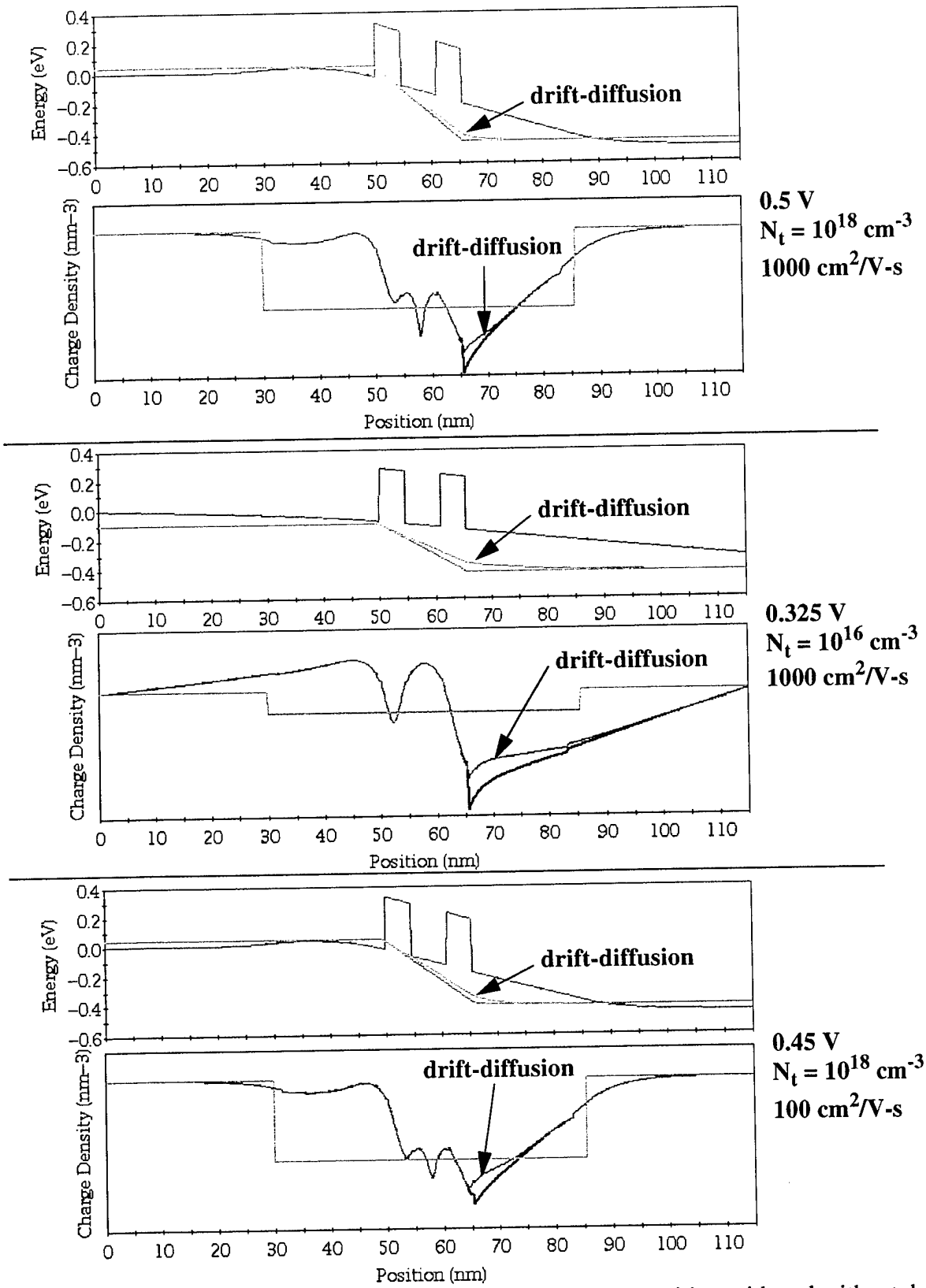

Figure 6-2. Conduction band edge and charge density plot versus position with and without drift diffusion in the terminals.

7.0 SUPERLATTICE STUDY

7.1 Superlattice Design Concerns

A THz device being developed at the University of California Santa Barbara (UCSB) is a Bloch oscillating miniband superlattice (Wanke et al., 1996, 1998; Zeuner et al., 1996; Schomburg et al., 1998; Sibille et al., 1994; Unterrainer et al., 1996). A Bloch oscillating miniband superlattice, is both a transport and a quantum transition device. Under strong electrical bias, quantum well states are pulled out of resonance forming a Stark ladder, the current density falls and transport can occur by making quantum transitions between the Stark split ground states of neighboring wells. (Figure 7-1(a)) There is no inversion, temperature has only secondary effects but enhanced gain occurs just below the Stark splitting (Loss occurs above.) Dynamics separate loss from gain.

Miniband superlattices in the AlGaAs system have been used (Keay et al., 1995) to demonstrate new phenomena that lay the foundation for the device physics used here: (a) multi-photon assisted tunneling, (b) dynamic localization, (c) absolute negative conductance and, (d) multi-photon resonance with Bloch oscillation.

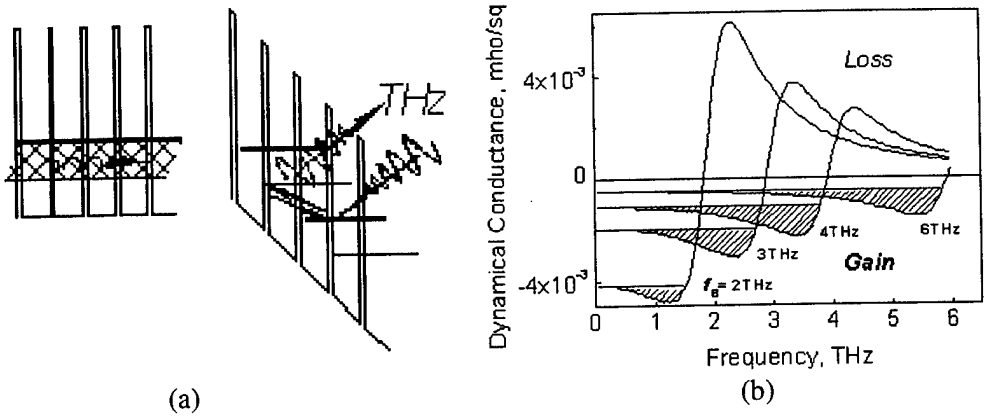

(a) (b)

Figure 7-1. (a) A schematic miniband super-lattice (left) breaks into a Stark ladder under bias (right). (b) Dynamical conductance of a quasi-optical array of miniband superlattice diodes. This is a 50 period AlGaAs/GaAs superlattice comprised of 8 nm quantum wells and 2 nm barriers producing a miniband width of 20 meV or ~5.5 THz, the intrinsic tunneling rate between quantum wells. The frequencies correspond to the Stark splitting between adjacent quantum wells. The cross hatched area represents the "available" gain.

There are important material features. (a) No inversion is required for gain. (b) The gain is enhanced near the Stark splitting and is voltage controlled (Gunn devices are limited to frequencies below the energy relaxation time). (c) Power combining takes place in the material. (In principal the gain of a 50 quantum well miniband superlattice will saturate at twice the THz field as a 25 quantum well miniband superlattice. Very roughly speaking, we have 50 very fast RTDs in series.). (d) Non-linearities are strong and THz fast. The devices will be power combined in quasi-optical arrays (York et al., 1997). The THz cavities will be loaded with these quasi-optical arrays to form an electrically driven solid state oscillator. The electron mini-bandwidth must be broad but less than the LO phonon energy, momentum scattering long, and mobility high.

Underlying device physics has been largely explored and cleanly demonstrated in the prototypical AlGaAs. There are better materials. InAs/AlSb/GaSb grown to the perfection of the AlGaAs system could make substantial improvements in the projected device performance. High optic phonon frequencies for the AlGaN materials (20 THz in the nitrides vs 10 THz for III-V s) make them very attractive. Doubling the optic phonon frequency opens the 10THz region by removing lattice absorption and reducing phonon mediated relaxation. Since NEMO can simulate a variety of material systems, it is a strong base upon which to develop simulation tools that optimize material as well as device configuration.

Fundamental to device operation are miniband superlattices that support ballistic electron transport over several superlattice periods. Coherence is essential. Heavily doped superlattices that limit transport to less than a period will exhibit I-V characteristics that mimic Bloch oscillation but will be controlled by energy relaxation and are "Gunn" like devices.

Figure 7-1(b) shows the calculated dynamical conductance versus frequency for an electrically biased superlattice in the Bloch limit where transport is limited by Bragg scattering. Each curve represents a different electric field, labeled by the Stark splitting between adjacent quantum wells. The feature that emerges is a steadily rising gain or negative dynamical conductance up to a frequency just below the Stark splitting (See Figure 7-1(a)) or Bloch frequency. The dynamical conductance refers to the sheet conductance of an appropriate quasi-optical array. "Gunn" effects and the aforementioned superlattice work in heavily doped superlattice material produce gain only at frequencies below the energy relaxation time ~100-200 GHz. But, here the cut-off frequency is the Stark splitting.

The negative resistance at DC is problematic and signals various field instabilities, which will be only compounded when the device is embedded in a quasi-optical array. But the gain rises with increasing frequency and we can shunt the negative conductance, at low frequencies by a positive conductance equal to the DC value, without extinguishing the resonant gain near the Stark splitting or Bloch frequency. Indeed, if the shunt behaves like a resistive element, its THz impedance can only increase with frequency leaving the THz gain, near the Stark splitting, exposed. In Figure 7-1(b) the cross hatch regions indicate the gain available after the material is shunted by a positive conductance to stabilize the DC bias.

7.2 Superlattice from University of California at Santa Barbara

NEMO was used to simulate a superlattice structure from the University of California at Santa Barbara (UCSB). The superlattice is grown on a GaAs substrate and uses the InAs/AlSb material system. The layer sequence of the grown superlattice is shown in Figure 7-2(a) and some experimental J-V measurements are shown in Figure 7-2(b).

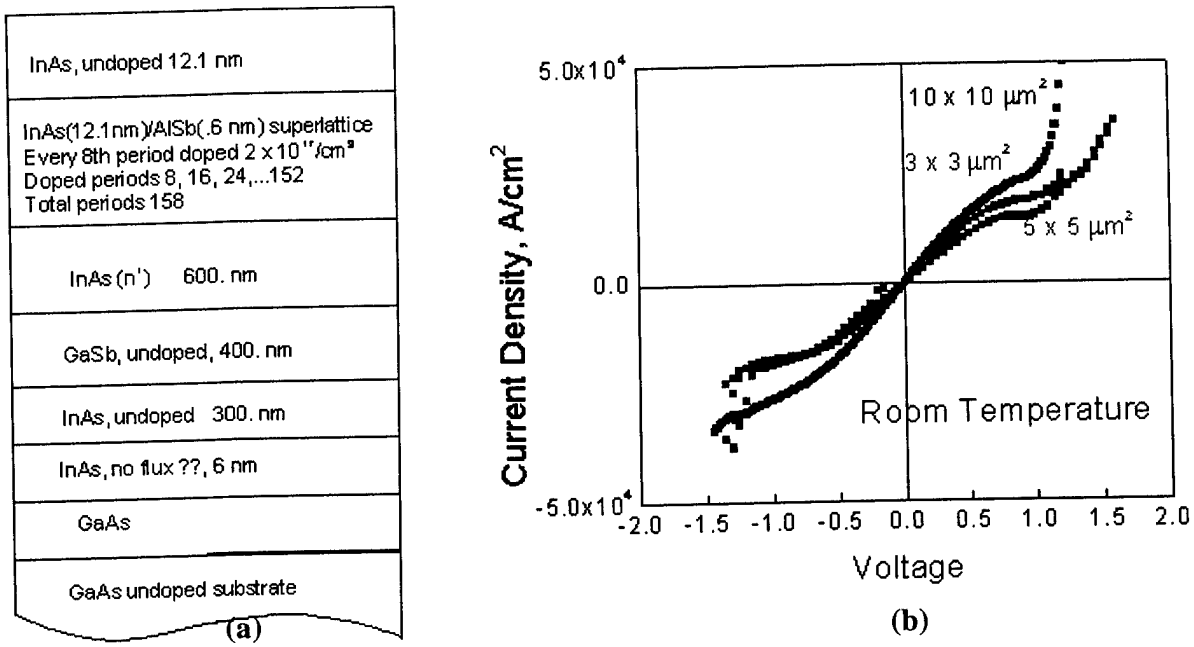

Figure 7-2. (a) Layer sequence of grown InAs/AlSb superlattice. (b) Measured J-V characteristics of superlattice for three different cross-sectional areas.

The superlattice geometry which was simulated is shown in Figure 7-3. When comparing with Figure 7-2(a) it should be noted that the simulated layer sequence shows no GaAs as well as some other material layers that were etched away when fabricating the device. NEMO is used to simulate only those device layers where carrier transport is occurring in the superlattice. The ML unit used here is half the lattice constant of InAs (0.30292 nm). NEMO allows only whole ML units for layer thicknesses so layer thicknesses may differ from those cited in Figure 7-2. Cited experimental distances have been rounded of to the nearest ML. The layer thickness (t) variation is assumed to be in the [111] lattice direction. All doping levels cited are donor number densities (N_D). The undoped carrier level was taken to be 5 x10^{16}. Also, none of the simulations used the number of superlattice periods of the experimental device (L_{SL} = 158). There is a memory limit to the number of periods NEMO can simulate.

	N_D (cm^{-3})	t (nm)	t (ML)	comments
InAs	3e+17	199.927	660	nemo "collector"
InAs	5e+16	12.1	40	
AlSb InAs	5e+16 5e+16	0.6 12.1	2 40	repeated L_{SL} periods, every 8th period InAs doped 2e+17
InAs	3e+17	199.927	660	nemo "emitter"

Figure 7-3. Layer sequence of simulated superlattice modeled after UCSB's InAs/AlSb superlattice device.

Shown in Figure 7-4 is an equilibrium calculation (zero applied voltage) of a L_{SL} = 64 InAs/AlSb superlattice. The Hartree potential was used to calculate the quantum charge throughout the superlattice. A simple parabolic single band model was used. The conduction band edge (black)

and fermi level (tan) versus position is plotted in Figure 7-4(a). The doping level (tan) and the charge density (black) is shown in Figure 7-4(b). The doping increases every eighth period as specified. The charge density goes through various maxima in the quantum wells throughout the superlattice corresponding to the high charge density in the highly doped regions (every eighth superlattice period). The charge density is large enough in these highly doped periods to perturb the electric potential as seen in Figure 7-4(c). Consequently, the static electric field also exhibits an oscillatory behavior on the order of +/- 10^{-3} V/nm.

NEMO cannot be used to calculate non-equilibrium features of the superlattice due to its inability to model carrier transport through the superlattice. Although NEMO can handle coherent transport through the superlattice, NEMO cannot currently model incoherent transport as well as scattering and phonon interactions through many quantum wells. The most NEMO can currently handle is transport through a double barrier.

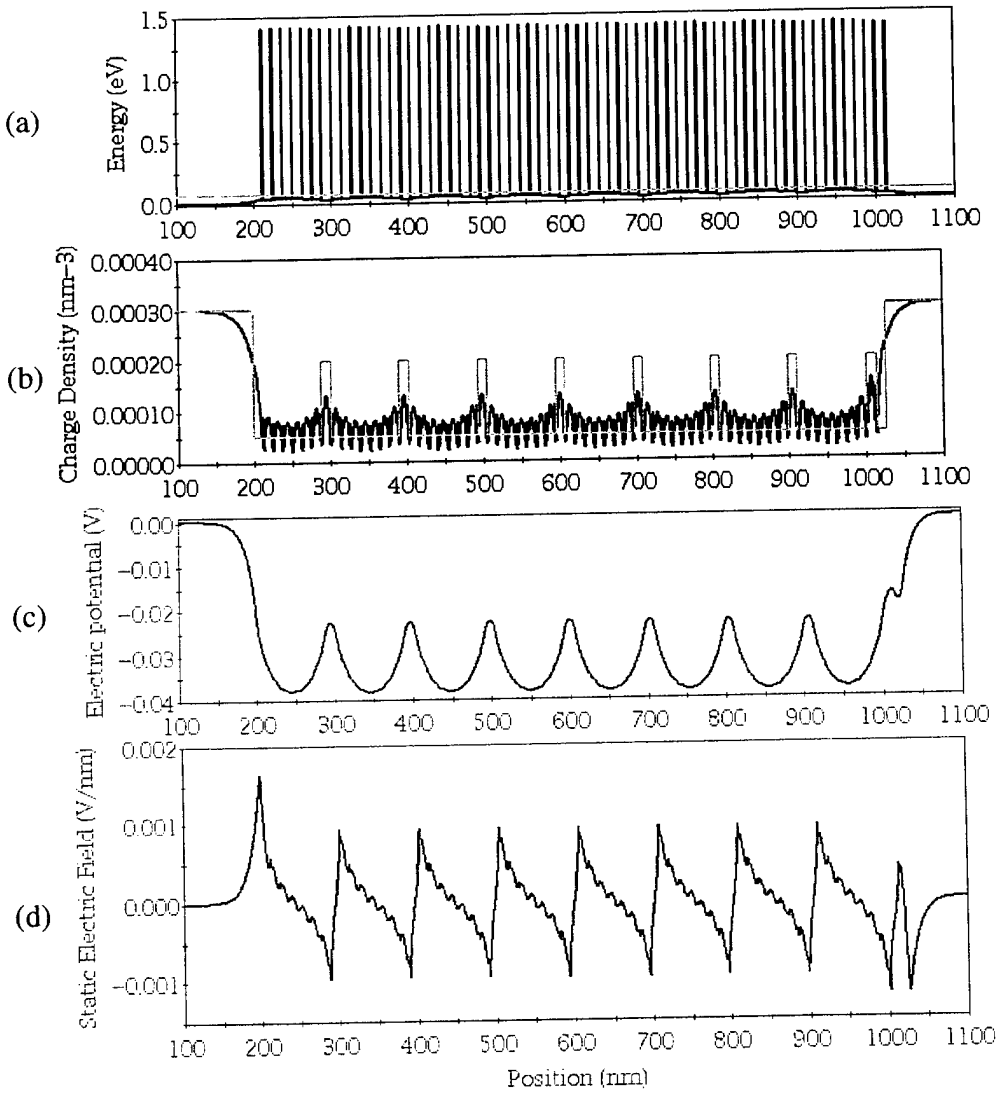

Figure 7-4. Equilibrium calculations for UCSB's InAs/AlSb superlattice (described in Figure 7-3) with L_{SL} = 64. Shown are the (a) conduction band edge, (b) doping profile and charge density, (c) electric potential, and (d) electric field.

8.0 QCL STUDY

The main goal of Phase I is to see what capabilities NEMO currently has to aid in THz device design and what modifications are needed to better address THz device modeling needs in the future. To this end a study was made of the Quantum Cascade Laser (QCL). This is an important terahertz device and will be a **long-term goal** for NEMO to model. The exercise here is to see what NEMO can solve now and what development will be needed in the future to model QCLs. Although the current model cannot calculate the light power out versus current (L-I), the model can calculate a subset of the semiconductor laser problem. For instance, the model can calculate quantities such as the eigenstates in the system, the wave functions, the electric potential, and the i-v characteristic of the device (including only coherent transport).

For example, NEMO was used to analyze the mid-infrared QCL discussed in (Sirtori et. al., 1997). The device is grown on an InP substrate and uses the $Ga_{0.47}In_{0.53}As$-$Al_{0.48}In_{0.52}As$ material system. The layer sequence of the waveguide cladding, waveguide core, and the Injector/Active region in the core is shown in Figure 8-1. The nominal width and length of this mesa etched ridge waveguide laser is 18 μm x 1.8 mm.

The layer sequence in Figure 8-1 has only one stage in the injector/active region. The ML unit used here is half the lattice constant of InP (0.293435 nm). NEMO allows only whole ML units for layer thicknesses so layer thicknesses here may differ from those cited in (Sirtori et. al., 1997). The graded areas are AlGaInAs with the In and Al mole fractions stepped in 3 ML intervals to transition from one material type to another.

InP substrate	1e+17 cm^{-3}	1000 nm	3408 ML	
Graded	1.2e+17	25	85	InGaAs, 3 ML x 28, In 0.0000-0.5320
InGaAs	6e+16	700.136	2386	
InAlAs	-	2.34748	8	
InGaAs	-	4.40153	15	
InAlAs	-	1.46718	5	
InGaAs	-	3.52122	12	
InAlAs	2e+17	1.17374	4	
InGaAs	2e+17	3.52122	12	
InAlAs	2e+17	1.17374	4	
InGaAs	2e+17	3.52122	12	
InAlAs	-	0.880305	3	
InGaAs	-	3.52122	12	
InAlAs	-	4.40153	15	
InGaAs	-	7.92274	27	
InAlAs	-	0.880305	3	
InGaAs	-	5.57526	19	
InAlAs	-	2.34748	8	
InGaAs	-	4.40153	15	
InAlAs	-	1.46718	5	
InGaAs	-	3.52122	12	

InAlAs	2e+17	1.17374	4	
InGaAs	2e+17	3.52122	12	
InAlAs	2e+17	1.17374	4	
InGaAs	2e+17	3.52122	12	
InAlAs	-	0.880305	3	
InGaAs	-	3.52122	12	
InGaAs	6e+16	500.013	1704	
Graded	2e17	39	132	AlGaInAs, 3 ML x 44, In 0.5318-0.5230, Al 0.0180 - 0.4770
InAlAs	1.2e+17	1199.86	4089	
InAlAs	3e+17	1199.86	4089	
Graded	5e+17	30	102	AlGaInAs, 3 ML x 34, In 0.5233 - 0.5317, Al 0.4638 - 0.0136
InGaAs	7e+18	600.075	2045	
InGaAs	1e+20	19.9536	68	

Figure 8-1. Layer sequence of simulated QCL.

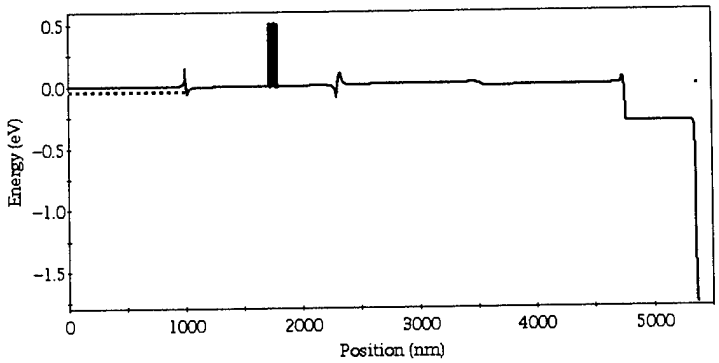

Figure 8-2. Erroneous conduction band edge calculation for QCL device. Shows the over prediction of band bending in the highly doped collector region where the parabolic density of states assumption breaks down.

The calculated conduction band edge for the whole device (cladding and core) is shown in Figure 8-2 and just the injector/active region with bound state energy levels in Figure 8-3. These calculation were done with the semi-classical models in NEMO. The semi classical free carrier density is calculated throughout the device using quasi-fermi levels. Within the terminals a constant quasi-fermi level is defined based on the doping and the band edges of the left most (right most) site of the left (right) terminal. In between the terminals the fermi levels are linearly interpolated. The fermi-levels are determined using a parabolic density of states effective mass approximation. The effective masses for the Γ conduction band are used.

If the whole QCL device is considered (cladding and core, Figure 8-2) the results are in error, as expected, when the simple semi-classical models are used. The band bending in the highly doped regions are over predicted when using the simple semi-classical models. That is, the simple parabolic density of states does not hold for these highly doped regions. The core and cladding band edges are compressed toward the fermi level. The highly doped collector region has pulled the fermi level unrealistically many eV above the conduction band edge.

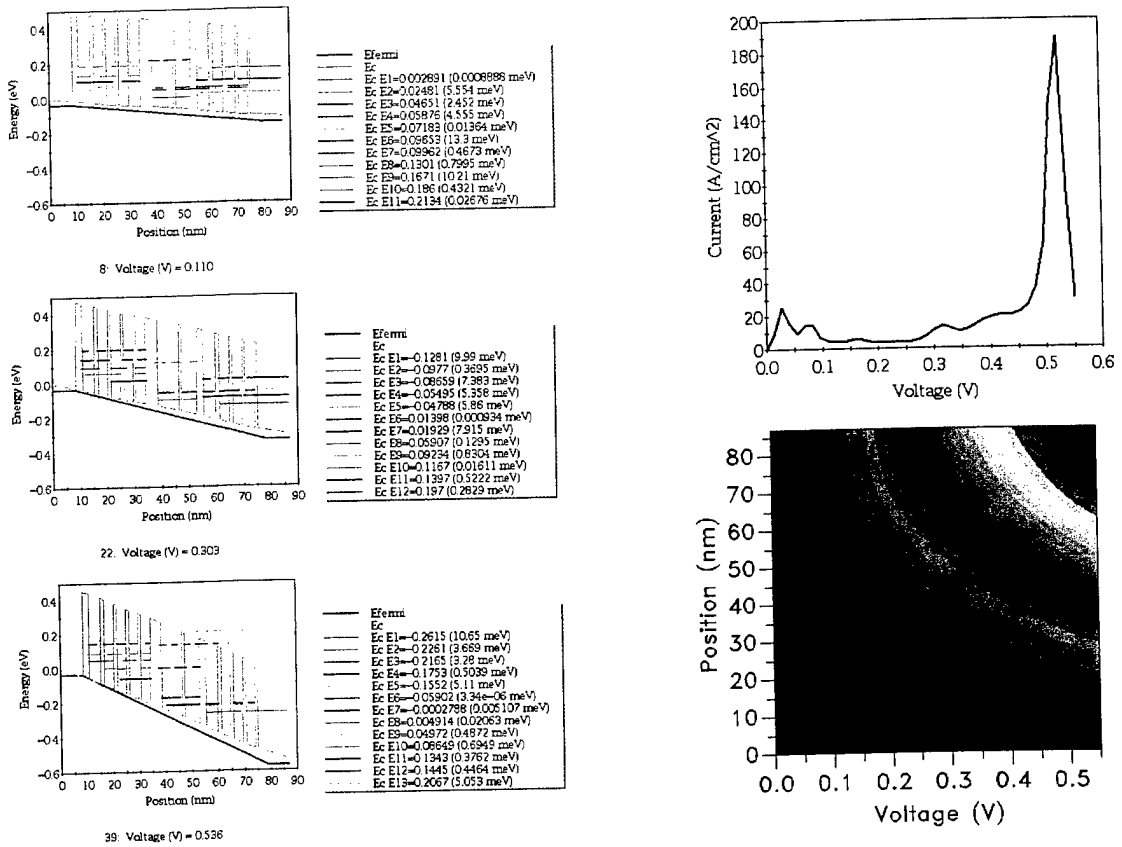

Figure 8-3. Conduction band edge with calculated energy levels, i-v curve, and electric potential versus position for the injector/active region.

NEMO was originally formulated to handle transport of carriers between two reservoirs of carriers through energy barriers where coherent transport is important. NEMO cannot handle incoherent transport through superlattices or transport through extended regions of semiconductors with no heterostructures present. Incoherent transport through the superlattice will need to be addressed in phase II work. Another deficiency in NEMO is that the quaternary used in the graded region has no band model parameters for the multi-band models in the material database. The multi-band models are typically used if non-parabolic density of states need to be calculated. The **k • p** multi-band model with the appropriate band model parameters will be tried in the second half of this project.

If just the injector/active region is simulated using the simple semi-classical models (Figure 8-3) the results are more reasonable. In the near term this is what NEMO has to offer designers of THz devices: a detailed quantum description of the superlattice region of the device (eigenstates, wavefunctions, quantum charge). Figure 8-3 shows the conduction band edge for three applied voltages, the electric potential, and the i-v curve. The QCL is operated under a positive bias corresponding to an average electric field of 6.2 x10^4 V/cm. For the spatial region of the device simulated in Figure 8-3 this is close to the 0.536 V voltage case (6.13 x10^4 V/cm). The energy level differences calculated are ΔE_{74} = 175 meV and ΔE_{43} = 41 meV which are near 145 meV and 41 meV cited in (Sirtori et. al., 1997). A parabolic single-band effective mass was used in the

calculations. The parabolic band assumption makes upper energy levels inaccurate. The semi-classical model also predicts a non-uniform electric field across the device with a slight increase of the electric field in the active region of the device.

In the terminals Thomas-Fermi statistics are used with non-varying (with position) fermi levels, Hartree self-consistency is used in the non-equilibrium regions. There is no scattering nor incoherent transport being modeled. The consequence of no scattering and only coherent transport can be seen in the electron density calculations shown in Figure 8-4. Neglecting scattering and incoherent transport under predicts the amount of carriers in the super lattice. Given no scattering and no incoherent transport NEMO can not handle transport through many injector/active stages. Figure 8-5 shows calculated conduction band edges and electron densities for multiple injector/ active regions at two different applied voltages. The "bowing" in the band diagram is a result of an insufficient number of free carriers in the superlattice.

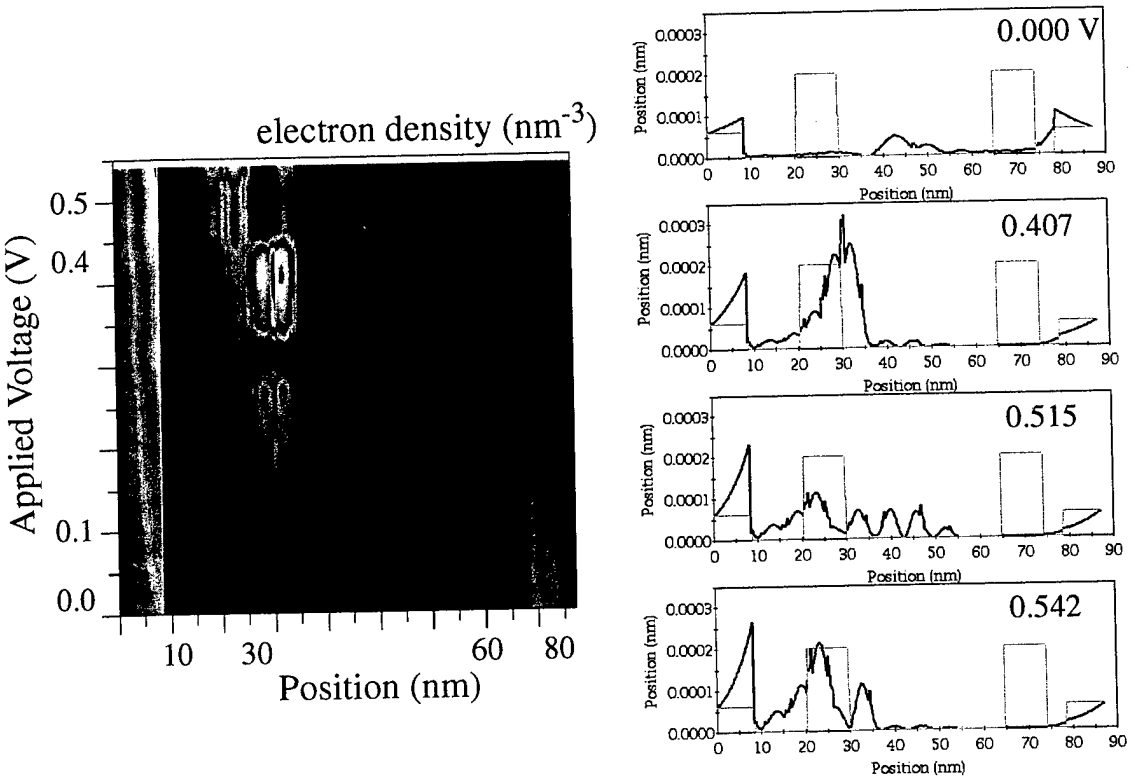

Figure 8-4. Electron density ($nm^{-3} = 10^{21}\ cm^{-3}$) versus position for varying applied voltage. Also, electron density and doping profile versus position at four different applied voltage slices.

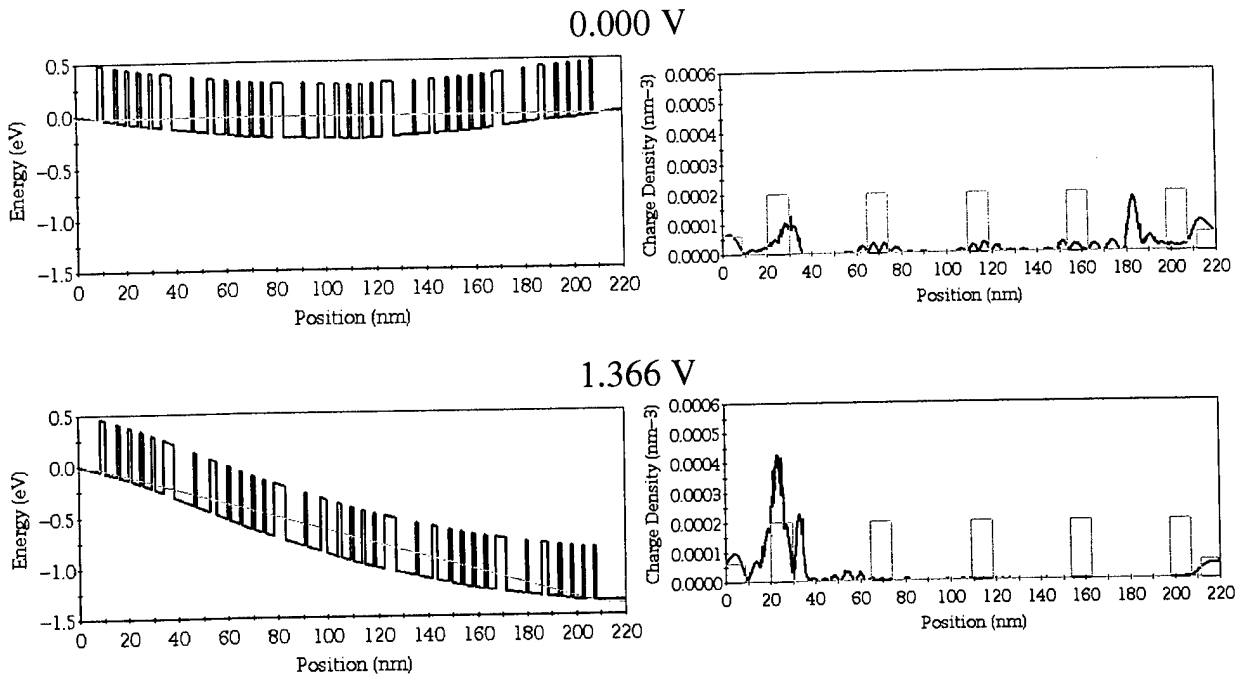

Figure 8-5. Conduction band edge, electron density ($nm^{-3} = 10^{21}\ cm^{-3}$), and doping levels versus position for two applied voltages and multiple injector/active stages.

9.0 COMMERCIALIZATION

CFDRC is committed to commercialize NEMO software. During the Phase I effort, the NEMO GUI is being transitioned to the FOX library. The GUI which is using third party widgets is being converted into a FOX based widget set. This free source CFDRC technology will enable tighter integration with other CFDRC products. The conversion will also allow the code to be run on windows platforms as well as the unix flavors the tool currently runs on.

A web site for marketing, training, support, and distribution has been established. The NEMO web pages which were formerly served by Raytheon are now on the CFDRC's web site (www.cfdrc.com/~nemo). Since the web site has been put on line approximately 20 unsolicited requests for more information have been received.

CFDRC will invest internal and sponsored (U.S. industry, DoD, . . .) resources to prepare the quantum tool for commercial sale and support. The documentation is being updated and put in a form conforming to CFDRC support staff requirements.

There are plans to advertise the CAD tool at exhibitions, conferences (eg., APS, IEEE, . . .), and in trade magazines.

An open development environment will be established for academic research (physics enhancements, validation, . . .) and interfaces to commercial TCAD tools will be developed.

A license to develop and sell NEMO is being finalized between Raytheon and CFDRC which gives CFDRC access to the latest NEMO source code, the right to develop and exclusively commercialize NEMO. Raytheon has also recognized JPL as an entity in which NEMO development can occur. Finally CFDRC is recognized by Raytheon as the caretaker of the "universal" source to be developed and marketed during the SBIR project.

10.0 CONCLUSIONS AND PLANS FOR FUTURE WORK

This chapter presents the conclusions from the current project and the plans for future extensions and applications of the Quantum CAD tool.

10.1 Summary of Accomplishments

The significant achievements during phase I of the project are an existing quantum simulator, NEMO, has been coupled to a drift-diffusion model to enable multi-scale studies of semiconductor devices. The quantum device simulator linked to a classical model has been demonstrated and verified on RTDs, superlattices, and QCLs with varying levels of success. Finally, the tool was further integrated into CFDRC's commercial microelectronics CAD environment by converting the GUI to FOX (a CFDRC GUI library technology).

In conclusion, the main development requirements for NEMO to model quantum based THz devices, which consist of multiple quantum wells, is the inclusion of incoherent transport processes and improving the material database. The incoherent tranport processes would include energy level transitions within quantum wells and scattering between energy levels as the carriers are transported through the multiple quantum wells. The material database improvements would include ternaries, InAs, AlSb, and SiGe. Not all of these materials presently have accurate parameters for the higher level band models.

10.2 Recommended Future Development, Validation, and Applications

There are several important needs for enhancing the Quantum CAD tool. Some of the most important improvements relevant for THz devices follow.

Rate equations for carrier transitions including energy relaxation and in-plane momentum scattering. To implement the carrier transitions each well in the superlattice will be discretized spatially with a single node for each well. Each spatial node will have 100-1000 transverse (in plane momenta) associated with it. Transitions can happen between spatial nearest neighbors among various in-plane transverse momenta (Klimeck et. al., 1994). The transport will be solved with an iterative scheme of the linear system. The transitional levels are already calculated in NEMO.

Material Database Development. When simulating the THz devices under this study, it became apparent the material database need to undergo improvements. To implement the classical transport models mobility needs to be added in the database. The mobility is a function of the material, ionized dopant density, the lattice temperature, the carrier temperatures, and the longitudinal and transverse electric fields. The mobilities for alloys such as **ternaries** and **quaternaries** needs to be researched. **Many of the bandstructure parameters are not available for all material systems.** For example, the sp3s* band model parameters are not defined in the code for SiGe and AlSb.

Time domain Green function model. Many Quantum devices will be incorporated into future digital circuits. In digital circuits the step response of the device is of great interest. To model the step response of Quantum devices such as RTDs one cannot use large signal AC. A full time

dependent simulation is necessary to analyze the step response of quantum devices. A general, non-equilibrium Green function, time-domain model could address this need. A general theory using a model Hamiltonian has been previously described by Wingreen, Jauho, and Meir [Wingreen et. al., 1993]. The theory can be rewritten for the localized orbital basis used in NEMOs bandstructure models and optimized for numerical implementation. The theoretical development would have 4 main components;

(i) Formulate the open system bulk boundary conditions.
(ii) Formulate the time-dependent generalized boundary conditions equivalent to those used in NEMO.
(iii) Develop the most efficient algorithms for calculating the current and charge across the device.
(iv) Formulate several different algorithms for including incoherent scattering from phonons, ionized impurities, interface roughness, and alloy disorder. The algorithms would trade off accuracy with numerical cost.

Implement small and large signal AC into an existing Quantum simulator. Circuit designers in the real world use the circuit simulator SPICE to design and analyze radio frequency (rf) circuits. The SPICE simulator uses equivalent lumped elements that mimic the actual devices to predict the behavior and effect the devices have in a complete circuit. The equivalent lumped element parameters are typically extracted from (i) the DC current-voltage curve and (ii) the frequency dependent S-parameter curve of the device. Both characteristics can be measured experimentally including parasitic device effects. Simulations which can calculate these two characteristics could also calculate equivalent lumped element parameterizations for use in SPICE. NEMO has already been proven to match well with experimental DC i-v curves of actual devices. The AC signal analysis could be incorporated into NEMO. Small signal AC analysis has already been demonstrated. The formulation for the large signal AC analysis which is charge self-consistent has been developed under a previous project. The AC analysis can be generalized and extended to large signal device response. The number of harmonics will vary. The open system boundaries [Klimeck et al., 1995; Lake et al., 1997] that makes NEMO so versatile can be enhanced to account for the higher order harmonics generated from the sinusoidal potential response. The AC charge can be calculated self-consistently with the AC potential. The total current (particle plus displacement) can be calculated and generated as output.

Automate compact model parameter extraction for circuit design. The equivalent lumped element parameters can be calculated from DC current voltage and S-parameter curves that were generated from NEMO. The circuit parameters or reduced models characterizing the device and made a function of frequency and voltage can be calculated automatically and optimized using optimization algorithms such as genetic algorithms (GAs).

Optical effects. To enable the characterization of THz detectors the AC model developed in the quantum simulator could be enhanced to include optical effects. The Hamiltonian developed for the electronic AC analysis can be altered slightly for optical analysis. Instead of using the term, $\mathbf{V}\cos(\omega t)$ in the Hamiltonian, one would use $\mathbf{p} \bullet \mathbf{A}\cos\omega t$. The change affects only the matrix elements that couple the harmonics in the Hamiltonian. This would enable the modeling of the current response of a device such as an RTD or superlattice illuminated by a laser (i.e., a THz receiver).

Inverse RTD design problem. Given some desired i-v characteristic an RTD design (layer number, thickness, mole fraction, material, and doping levels) will be calculated which exhibits the desired characteristics. A genetic algorithm-based approach to back RTD structural information out of the RTD current-voltage characteristic could be used.

Increase Quantum Simulator from 1D to 2D. Increasing the number of dimensions in the quantum simulator will require fundamental changes to the structure of the code. Issues that will need to be addressed include the inclusion of side wall depletion, electron recombination and charging at surface states, multidimensional electron energy state distribution, band structure, and multidimensional effects on electron scattering. Also, increasing the spatial dimension in quantum simulator from 1D to 2D requires new meshing paradigms, infrastructure, numerical solvers, theory reformulation, and GUI modifications. Also, increasing the quantum simulator from 1D to 2D will allow the inclusion of a third contact.

Integrate NEMO into CFDRC commercial technologies. To enhance the calculation speed the linear equations and eigenvalue problems in the code solved using the freeware linear algebra package (LAPACK) can be transitioned to numerical solvers at use at CFDRC. The output data formats can be transitioned to an open standard (www.cfdrc.com/~DTF/). The Graphic User Interface (GUI) can be transitioned to the use of FOX libraries which are open source libraries (Free Objects for X, www.cfdrc.com/FOX/fox.html). This would allow a cross-platform GUI design from a single source and allow tighter integration with other CFDRC software. FOX is a C++ based tool kit for quickly developing fast, low memory, platform independent Graphical User Interfaces. The internal structure of the tool an be rewritten to provide a clear software interface between the solver and GUI.

Couple Quantum simulator to a classic device physics model such as a hydrodynamic or Boltzmann formulation. Currently, the Quantum simulator models the emitter and collector contacts as a reservoir of carriers in thermal equilibrium with the lattice. This approximation works well for degenerately doped semiconductors. However, for thin or moderately doped contacts this approximation begins to break-down. The electron and hole transport can be calculated using a hydronamic or Boltzmann formulation instead of assuming a thermalized sea of electrons. Thus effects such as carrier heating and non-local effects can be properly modeled. Linking the Quantum simulator with classical semiconductor device tools will allow complete multi-scale modeling solutions of quantum devices utilizing the computationally costly Quantum simulator only in the quantum regions.

11.0 REFERENCES

J.A. del Alamo, C.C. Eugster, Q. Hu, M.R. Melloch, and M.J. Rooks, "Electron Waveguide Devices", Superlatt. and Microstruct. **23**: 121 (1998).

W. A. Beck and T. S. Faska, "Current status of quantum well focal plane arrays", Proc. SPIE vol. **2744** pp. 192-206 (1996).

Blanks, D., Klimeck, G., Lake, R., Bowen, C., Frensley, W.R., Leng, M., and Fernando, C.L., Nanoelectronic Modeling (NEMO): A New Quantum Device Simulator, Second NASA Device Modeling Workshop, Moffett Field, pp. 70-84 (1997).

J. Faist, F. Capasso, C. Sirtori, D. L. Sivco, J. N. Baillargeon, A. L. Hutchinson, S. N. G. Chu and A. Y. Cho, Appl. Phys. Lett. **68** pp. 3680-3682 (1996)

Fernando, C. L., and Frensley, W. R., "Intrinsic high-frequency characteristics of tunneling heterostructure devices", Phys. Rev. **B 52** (7) pp. 5092-5104 (1995).

Qing Hu, G. de Lange, et. al., "Millimeter wave, terahertz, and infrared devices", Massachusetts Institute of Technology, Research Laboratory of Electronics Progress Report **141**, Part I, Section 3, Chap 3, pp. 145-150 (1998).

R. F. Kazarinov and R. A. Suris, Fiz. Tekh. Poluprovodn **5** pp. 797-800 (1971).

B.J. Keay, S. Zeuner, S.J. Allen, Jr.; K.D. Maranowski, A.C. Gossard, U. Bhattacharya, M.J.W. Rodwell, "Dynamic localization, absolute negative conductance, and stimulated, multiphoton emission in sequential resonant tunneling semiconductor superlattices", Phys. Rev. Lett. **75**, 4102 (1995).

G. Klimeck, R. Lake, S. Datta, and G. Bryant, "Elastic and Inelastic Scattering in Quantum Dots in the Coulomb Blockade Regime", Phys. Rev. B **50** , p. 5484 (1994).

Klimeck, G., Lake, R., Bowen, R.C., Frensley, W.R., and Blanks, D., IEEE 53rd Annual Device Research Conference Digest, p. 52 (1995a).

Klimeck, G. Lake, R., Bowen, R. C., and Frensley, W. R., "Quantum device simulation with generalized tunneling formula", Appl. Phys. Lett. **67** (17) pp. 2539-2541 (1995)

Klimeck, G., et al., "Tight-Binding Models for Si Quantum Devices and Parameter Fitting using Genetic Algorithms", accepted for publication in Superlattices and Microstructures (1999).

Klimeck, G., et al., "Genetically Engineered" Nanostructure Devices, accepted for publication in proceedings "Materials in Space Science, Technology, and Exploration", MRS Symposium Proceedings Vol. 551 (1999).

Lake, R., Klimeck, G., Bowen, R. C., and Jovanovic D., "Single and multiband modeling of quantum electron transport though layered semiconductor devices", J. Appl. Phys. **81** (12) pp.7845-7869 (1997)

LI. Lyubomirsky, and Q. Hu. "Energy Level Schemes for Far infrared Quantum Well Lasers", Appl. Phys. Lett. **73**: 300 (1998).

I. Lyubomirsky, Q. Hu, and M.R. Melloch, "Measurement of Far-infrared Intersubband Spontaneous Emission from Optically Pumped Quantum Wells", Appl. Phys. Lett. **73**: 3043 (1998).

Moise, T. S., Kao, Y.-C., Katz A. J., Broekaert, T. P. E., and Celii, F. G., J. Appl. Phys. **78** p. 6305 (1995).

Reddy, M., Martin, S.C., Molnar, A.C., Muller, R.E., Smith, R.P., Siegel, P.H., Mondry, M.J., Rodwell, M.J.W., Kroemer, H., Allen, S.J., Jr., "Monolithic Schottky-collector resonant tunnel diode oscillator arrays to 650 GHz" , IEEE Electron Device Lett. **18**, 218 (1997).

E. Schomburg, J. Grenzer, K. Hofbeck, T. Blomeier, S. Winnerl, S. Brandl, A.A. Ignatov, K.F. Renk, D.G. Pavelev, Yu Koschurinov, V. Ustinov, A. Zhukov, A. Kovsch, S. Ivanov, P.S. Kopev, "Millimeter wave generation with a quasi planar superlattice electronic device.", Solid-State Electron. **42**, 1495 (1998).

C. Sirtori, J. Faist, F. Capasso, D. L. Sivco, A. L. Hutchinson, and A. Y. Cho, "Mid-Infrared (8.5 mm) semiconductor lasers operating at room temperature", IEEE Photonics Technol. Lett. **9** pp. 294-6 (1997)

R. Stratton, "Semiconductor current-flow equations (diffusion and degeneracy)", IEEE Trans. Electron Dev. **ED-19** pp. 1288-1292 (1972).

K. Unterrainer, B.J. Keay, M.C. Wanke, S.J. Allen, D. Leonard, G. Medeiros-Ribeiro, U. Bhattacharya, M.J.W. Rodwell, "Inverse Bloch oscillator: strong terahertz-photocurrent resonances at the Bloch frequency", Phys. Rev. Lett., **76**, 2973 (1996).

M.C. Wanke, "Terahertz harmonic generation from Bloch oscillating superlattices in quasi-optical arrays", UCSB Ph.D. Dissertation, September (1998).

M.C. Wanke, S.J. Allen, K. Maranowski, G. Medeiros-Ribeiro, A.C. Gossard, P. Petroff, "Third harmonic generation in a GaAs/AlGaAs superlattice in the Bloch oscillator regime", Proceedings of 23rd International Conference on the Physics of Semiconductors, Edited by: M. Scheffler, and R. Zimmermann, R.. Singapore: World Scientific vol.**3** p.1791-4 (1996)

Wingreen, N.S., Jauho, A.-P., Meir, Y., Time-dependent Transport Through a Mesoscopic Structure , Physical Review B (Rapid Communications) **48**, pp. 8487-8490 (1993).

B. Xu, Q. Hu, and M. R. Melloch, "Electrically pumped tunable terahertz emitter based on intersubband transition", Appl. Phys. Let. **70** (1997).

R.York and Z. Popovic, eds., Active and Quasi-Optical Arrays for Solid-State Power Combining, Wiley: New York, (1997)

S. Zeuner, B.J. Keay, S.J. Allen, K.D. Maranowski, A.C. Gossard, U. Bhattacharya, M.J.W. Rodwell, "Transition from classical to quantum response in semiconductor superlattices at THz frequencies", Phys. Rev. B, Condens. Matter, 53, R1717 (1996).